# Trans-Pacific transport and evolution of aerosols: Evaluation of quasi-global WRF-Chem simulation with multiple observations

[1,2]Zhiyuan Hu, [2]Chun Zhao, [1]Jianping Huang, [2]L. Ruby Leung, [2]Yun Qian, [3,4]Hongbin Yu, [5]Lei Huang, [5]Olga V. Kalashnikova

[1]Key Laboratory for Semi-Arid Climate Change of the Ministry of Education, Lanzhou University, Gansu, China

[2]Atmospheric Sciences and Global Change Division, Pacific Northwest National Laboratory, Richland, WA, USA

[3]Earth System Science Interdisciplinary Center, University of Maryland, MD, USA

[4]Earth Science Division, NASA Goddard Space Flight Center, MD, USA

[5]Jet Propulsion Laboratory, California Institute of Technology and NASA, Pasadena, CA, USA

Manuscript for submission to *WRF-Chem special issue in Geosci. Model Dev.*

*Corresponding authors:

Chun Zhao, phone: (509) 371-6372; email: chun.zhao@pnnl.gov

## Abstract

A fully coupled meteorology-chemistry model (WRF-Chem, the Weather Research and Forecasting model coupled with chemistry) has been configured to conduct quasi-global simulation for the 5 years of 2010-2014 and evaluated with multiple observation datasets for the first time. The evaluation focuses on the simulation over the trans-Pacific transport region using various reanalysis and observational datasets for meteorological fields and aerosol properties. The simulation generally captures the overall spatial and seasonal variability of satellite retrieved aerosol optical depth (AOD) and absorbing AOD (AAOD) over the Pacific that is determined by the outflow of pollutants and dust and the emissions of marine aerosols. The assessment of simulated extinction Angstrom exponent (EAE) indicates that the model generally reproduces the variability of aerosol size distributions as seen by satellites. In addition, the vertical profile of aerosol extinction and its seasonality over the Pacific are also well simulated. The difference between the simulation and satellite retrievals can be mainly attributed to model biases in estimating marine aerosol emissions as well as the satellite sampling and retrieval uncertainties. Compared with the surface measurements over the western U.S., the model reasonably simulates the observed magnitude and seasonality of dust, sulfate, and nitrate surface concentrations, but significantly underestimates the peak surface concentrations of carbonaceous aerosol likely due to model biases in the spatial and temporal variability of biomass burning emissions and secondary organic aerosol (SOA) production. A sensitivity simulation shows that the trans-Pacific transported dust, sulfate, and nitrate can make significant contribution to surface concentrations over the rural areas of the western U.S., while the peaks of carbonaceous aerosol surface concentrations

46 are dominated by the North American emissions. Both the retrievals and simulation show
47 small interannual variability of aerosol characteristics for 2010-2014 averaged over three
48 Pacific sub-regions. The evaluation in this study demonstrates that the WRF-Chem quasi-
49 global simulation can be used for investigating trans-Pacific transport of aerosols and
50 providing reasonable inflow chemical boundaries for the western U.S. to further
51 understand the impact of transported pollutants on the regional air quality and climate
52 with high-resolution nested regional modeling.
53
54

# 1 Introduction

Aerosols, including from natural and anthropogenic sources in Europe, North Africa, and East Asia, can be transported across the Pacific Ocean thousands of miles downwind to North America and even beyond. Previous studies using ground-based and satellite measurements and numerical models have estimated about 7-10 days of travel time for aerosols to traverse the Pacific Ocean (Eguchi et al., 2009). Previous studies have shown that aerosols outflowed from the Asian continent could be transported by the mid-latitude prevailing westerlies across the Pacific Ocean and ultimately reach the west coast of North America and beyond, and its efficiency is the largest in spring (e.g., Takemura et al., 2002; Chin et al., 2007; Huang et al., 2008; Yu et al., 2008; Uno et al., 2009, 2011; Alizadeh-Choobari et al., 2014). Takemura et al. (2002) found that the contribution of anthropogenic aerosols to the total aerosol optical thickness is comparable to that of dust during the transport over the North Pacific in spring. Chin et al. (2007) found that the long-range transported dust brought 3 to 4 times more fine particles than anthropogenic pollutants to the total surface fine particles over the U.S. on annual average with a maximum influence in spring and over the northwestern U.S. Yu et al. (2008) estimated that about 25% of the Asian outflow reaches the west coast of North America, which is about 15% of the total North American emissions, and the transport fluxes are largest in spring and smallest in summer. Uno et al. (2011) also revealed that the dust trans-Pacific path sometimes could be split into two branches: a southern path to the central U.S. and a northern path that is trapped and stagnant for a longer time and finally subsides over the northwestern U.S.

These trans-Pacific aerosols can play an important role in atmospheric composition (e.g., Yu et al., 2008), air quality (e.g., Jaffe et al., 1999; VanCuren, 2003; Heald et al., 2006; Chin et al., 2007; Fischer et al., 2009; Yu et al., 2012; Tao et al., 2016), and regional weather and climate (e.g., Lau et al., 2008; Eguchi et al., 2009; Yu et al., 2012; Creamean et al., 2013; Fan et al., 2014; Huang et al., 2006, 2014) over the U.S. West Coast. At the surface, Heald et al. (2006) found that Asian anthropogenic aerosol plume increased aerosol concentrations in elevated regions of the northwestern U.S. by 0.16 $\mu g\ m^{-3}$ in spring 2001. Chin et al. (2007) also found that long-range transported dust increased the annual mean fine particle concentrations by 0.5-0.8 $\mu g\ m^{-3}$ over the western U.S., with a maximum enhancement in spring. The trans-Pacific transported aerosols can also significantly absorb and scatter solar radiation (Yu et al., 2012; Fast et al., 2014; Tao et al., 2016), and serve as cloud condensation nuclei and ice nuclei that affect winter storms in the western U.S. (Sassen, 2002; Ault et al., 2011; Creamean et al., 2013; Fan et al., 2014). Deposition of the transported aerosols on/into snowpack in elevated regions (Hadley et al., 2010) may also accelerate snowmelt and influence the regional hydrological cycle and climate over the western U.S. (Qian et al., 2009 and 2015; Painter et al., 2010). Hence it is important to quantify the trans-Pacific transport of aerosols and how they evolve over the long distance.

Previous studies have used global models to quantify the long-range transport of aerosols to the western U.S. (e.g., Fairlie et al., 2007; Heald et al., 2006; Chin et al., 2007; Hadley et al., 2007). However, simulations were performed at relatively coarse resolutions (typically 1-2 degrees) that cannot fully resolve the large geographical variability of aerosols over the western U.S. with complex topography (Zhao et al.,

100 2013a). Coarse resolution simulations also lack the capability to fully resolve aerosol-
101 cloud-precipitation interaction. Some studies have reported regional simulations at
102 relatively high resolutions over the western U.S. (e.g., Zhao et al., 2013a; Fan et al.,
103 2014; Fast et al., 2014). However, most of them either used sparse in-situ observations to
104 provide lateral boundary conditions that are only suitable for idealized or short-term
105 sensitivity studies, or used simulations from global models with inconsistent physics and
106 chemistry schemes to provide lateral boundary conditions, which introduce biases in
107 estimating the contribution and effect of trans-Pacific transported aerosols.

108 To investigate the impact of trans-Pacific transported aerosols on regional air
109 quality and climate of the U.S. West Coast, a multi-scale modeling framework including
110 global simulation at coarse resolutions that captures the large-scale circulation and
111 provides consistent chemical lateral boundaries for nested regional simulation at high
112 resolutions is needed. WRF-Chem, the Weather Research and Forecasting (WRF) model
113 (Skamarock et al., 2008) coupled with a chemistry component (Grell et al., 2005), is such
114 a modeling framework. As a state-of-the-art model, WRF-Chem supports nested
115 simulations, and includes complex aerosol processes and interactions between aerosols
116 and radiation, clouds, and snow albedo (Zhao et al., 2014). The model has been used
117 extensively to study aerosols and their impacts on air quality and climate at regional
118 scales (e.g., Fast et al., 2006, 2009; Gustafson et al., 2007; Qian et al., 2010; Gao et al.,
119 2011, 2014; Shrivastava et al., 2011; Chen et al., 2013, 2014; Zhao et al., 2010, 2011,
120 2012, 2013a; 2014). Zhao et al. (2013b) is the first study to use WRF-Chem for quasi-
121 global (180° W-180° E, 60° S-70° N) simulations at a resolution of 1° × 1° to examine
122 uncertainties in simulating global dust mass balance and radiative forcing.

Although the quasi-global WRF-Chem simulation described by Zhao et al. (2013b) has been used to provide realistic chemical lateral boundary conditions for multiple regional modeling studies (e.g., Zhao et al., 2014; Fan et al., 2015), its evaluation has not been documented so far. In this study, the WRF-Chem simulation for 2010-2014 is evaluated extensively using observational data. For lack of in-situ observations over East Asia and the Pacific Ocean during our simulation period, evaluation is performed mainly using reanalysis and satellite retrieval (e.g., CALISPO, MODIS, and MISR) datasets, along with some available ground-based observations from AERONET and IMPROVE in the region. We focus on the simulation over the trans-Pacific transport region as a first step to evaluate the simulation for providing consistent lateral chemical boundaries for nested regional simulations used to investigate the impact of transported aerosols on regional air quality and climate. Spatial evolution of aerosols during the trans-Pacific transport as well as their seasonal and annual variability simulated by WRF-Chem will also be characterized.

In the following sections, the detailed setup of WRF-Chem will be described in Section 2. In Section 3 ground-based measurements and satellite retrievals will be presented. In Section 4, we evaluate the WRF-Chem simulated spatial distributions and seasonal and annual variability of aerosols across the Pacific with the observations. The conclusion can be found in Section 5.

# 2 Model description

## 2.1 WRF-Chem

In this study, WRF-Chem (3.5.1), updated by scientists at Pacific Northwest National Laboratory (PNNL), is used. The MOSAIC (Model for Simulation Aerosol Interactions and Chemistry) aerosol module (Zaveri et al., 2008) coupled with the CBM-Z (carbon bond mechanism) photochemical mechanism (Zaveri and Peters, 1999) in WRF-Chem is selected in this study. MOSAIC uses a sectional approach to represent aerosol size distributions with four or eight discrete size bins in the current version of WRF-Chem (Fast et al., 2006). All major aerosol components including sulfate ($SO_4^{-2}$), nitrate ($NO_3^-$), ammonium ($NH_4^+$), black carbon (BC), organic matter (OM), sea-salt, mineral dust, and other inorganic matter (OIN) are simulated in the model. The MOSAIC aerosol scheme includes physical and chemical processes of nucleation, condensation, coagulation, aqueous phase chemistry, and water uptake by aerosols. Dry deposition of aerosol mass and number is simulated following the approach of Binkowski and Shankar (1995), which includes both turbulent diffusion and gravitational settling. Wet removal of aerosols by grid-resolved stratiform clouds and precipitation includes in-cloud removal (rainout) and below-cloud removal (washout) by impaction and interception, following Easter et al. (2004) and Chapman et al. (2009). Cloud-ice-borne aerosols through ice nucleation of aerosols are not considered in the model, but the removal of aerosols by the droplet freezing process is considered. Convective transport and wet removal of aerosols by cumulus clouds follow Zhao et al. (2013b).

Aerosol optical properties such as extinction, single scattering albedo (SSA), and asymmetry factor for scattering are computed as a function of wavelength for each model grid box. Aerosols are assumed internally mixed in each bin (i.e., a complex refractive index is calculated by volume averaging for each bin for each chemical constituent of

aerosols). The Optical Properties of Aerosols and Clouds (OPAC) data set (Hess et al., 1998) is used for the shortwave (SW) and longwave (LW) refractive indices of aerosols, except that a constant value of 1.53+0.003i is used for the SW refractive index of dust following Zhao et al. (2010, 2011). A detailed description of the computation of aerosol optical properties in WRF-Chem can be found in Fast et al. (2006) and Barnard et al. (2010). Aerosol radiative feedback is coupled with the Rapid Radiative Transfer Model (RRTMG) (Mlawer et al., 1997; Iacono et al., 2000) for both SW and LW radiation as implemented by Zhao et al. (2011). The optical properties and direct radiative forcing of individual aerosol species in the atmosphere are diagnosed following the methodology described in Zhao et al. (2013a). Aerosol-cloud interactions were included in the model by Gustafson et al. (2007) for calculating the activation and resuspension between dry aerosols and cloud droplets.

**2.2 Numerical experiments**

Following Zhao et al. (2013b), we use a quasi-global channel configuration with periodic boundary conditions in the zonal direction and 360 × 145 grid cells (180° W-180° E, 67.5° S-77.5° N) to perform simulation at 1° horizontal resolution over the period 2010-2014. Alizadeh-Choobari et al. (2015) conducted a global WRF-Chem simulation of dust and its radiative forcing, which was configured with dust aerosol only without other aerosols and chemistry. However, WRF-Chem global simulation with sophisticated chemistry including anthropogenic and natural aerosols could not run stably due potentially to convergence issue of solving chemical reactions near the relatively pristine polar regions. Given the need of sophisticated chemistry to simulate not only dust but also other anthropogenic aerosols, a more stable near global coverage WRF-Chem

191 configuration is used in this study to circumvent this technical difficulty to characterize
192 the trans-Pacific transport of aerosols. The simulation is configured with 35 vertical
193 layers up to 50 hPa. The meteorological initial and lateral meridional boundary
194 conditions are derived from the National Center for Environmental Prediction final
195 analysis (NCEP/FNL) data at 1° horizontal resolution and 6 h temporal intervals. The
196 modeled wind components u and v and atmospheric temperature are nudged towards the
197 NCEP/FNL reanalysis data throughout the domain with a nudging timescale of 6 h in all
198 cases (Stauffer and Seaman, 1990). This provides a more realistic simulation of large-
199 scale circulation, which is important for modeling long-range transport. The chemical
200 initial and meridional boundary conditions are taken from the default profiles in WRF-
201 Chem, which are the same as those used by McKeen et al. (2002) and are based on
202 averages of mid-latitude aircraft profiles from several field studies over the eastern
203 Pacific Ocean. The impact of chemical boundary conditions on the simulated results is
204 negligible (Zhao et al. 2013b). This study uses a set of selected schemes for model
205 physics, including the MYJ (Mellor–Yamada–Janjic) planetary boundary layer scheme,
206 Noah land surface scheme, Morrison 2-moment microphysics scheme, Kain-Fritsch
207 cumulus scheme, and RRTMG longwave and shortwave radiation schemes.

208 **2.3 Emissions**

209 Anthropogenic emissions are obtained from the REanalysis of the TROpospheric
210 (RETRO) chemical composition inventories (http://retro.enes.org/index.shtml) except
211 over East Asia and the United States. Over the U.S., the National Emission Inventory
212 (NEI) 2011 is used. Over East Asia, the Asian emission inventory described by Zhang et
213 al. (2009) at 0.5°x0.5° horizontal resolution for 2006 is used except that BC, OM, and

sulfate emissions over China are from the China emission inventory for 2010 described by Lu et al. (2011) at a 0.1°x0.1° horizontal spatial resolution and a monthly temporal resolution for the simulation period. Biogenic emissions are calculated following Guenther et al. (1994). Biomass burning emissions are obtained from the Global Fire Emissions Database, Version 3 (GFEDv3) with monthly temporal resolution (van der Werf et al., 2010) and vertically distributed following the injection heights suggested by Dentener et al. (2006) for the Aerosol Comparison between Observations and Models (AeroCom) project. The WRF-Chem code is modified to update the biomass burning emissions every day. Sea-salt emission follows Zhao et al. (2013a), which is based on Gong (2003) to include correction of particles with radius less than 0.2 μm and Jaegle et al. (2011) to include the sea-salt emission dependence on sea surface temperature. Vertical dust emission fluxes are calculated with the Goddard Chemical Aerosol Radiation Transport (GOCART) dust emission scheme (Ginoux et al., 2001), and the emitted dust particles are distributed into the MOSAIC aerosol size bins following a theoretical expression based on the physics of scale-invariant fragmentation of brittle materials derived by Kok (2011). For MOSAIC 8-bin, dust particles are emitted into eight size bins with mass fractions of $10^{-6}$%, $10^{-4}$%, 0.02%, 0.2%, 1.5%, 6%, 26%, and 45%, respectively. Although the main purpose of this study is to evaluate the WRF-Chem simulation, a sensitivity simulation, in which dust, fire, and anthropogenic emissions over North America (10°N-70°N and 170°W-60°W) are removed, is also conducted to understand the contribution of trans-Pacific transported aerosols to the surface aerosol concentrations over the western U.S.

# 3 Aerosol Observations

## 3.1 Satellite Retrievals

### 3.1.1 MODIS

The Moderate Resolution Imaging SpectroRadiometer (MODIS) instrument onboard the NASA EOS Terra satellite observes Earth in 36 spectral bands from 0.4 to 14.4 μm, and provides nearly daily global coverage with local equatorial overpass time of about 10:30 AM since 2000 (King et al., 1999). The "dark target" algorithm has been developed to retrieve AOD and size parameters (Angstrom exponent, effective radius, and fine-mode fraction) over waters and vegetated lands (Kaufman et al., 1997; Remer et al., 2005). The "deep blue" algorithm has been implemented to retrieve AOD over bright land initially, which then has also been extended to vegetated land (Hsu et al., 2006, 2013). MODIS aerosol products have been widely used to characterize the regional, seasonal, and global distribution of aerosol and its components (Yu et al., 2003, 2009; Chin et al., 2004; Kaufman et al., 2005a), estimate aerosol radiative forcing (Yu et al., 2004; Remer and Kaufman, 2006), and study aerosol-cloud interactions (Kaufman et al., 2005b; Koren et al., 2005; Yu et al., 2007). In this study, MODIS data from the collection 5.1 are used. We use the "deep blue" AOD over land and the "dark target" AOD over ocean, both at 550 nm and at 1° x 1° horizontal resolution. Also, we use the "dark target" over-ocean extinction Angstrom exponent (EAE) over the 470-660 nm wavelength range to evaluate model simulations of particle size information (Anderson et al., 2005; Remer et al., 2005; Levy et al., 2013).

### 3.1.2 MISR

259 The Multi-angle Imaging SpectroRadiometer (MISR) instrument onboard the
260 Terra spacecraft crosses the equator at ~10:30 AM local time since 1999. It observes
261 continuously in four narrow spectral bands centered at 446, 558, 672 and 866 nm using
262 nine separate cameras oriented along the orbital track with surface viewing zenith angles
263 ranging from ±70.5° (Diner et al., 1998). Aerosol retrievals are performed on 16 × 16
264 patches of 1.1 km sub-regions, yielding an aerosol product at 17.6 ×17.6 km spatial
265 resolution, referred to as a "Level 2" product (Martonchik et al., 2002). MISR Level 2
266 aerosol products have been described in Kahn et al (2009). The latest version (Version 22)
267 of MISR aerosol product also provides the fraction of AOD due to "fine" (particle radii
268 <0.35 μm), "medium" (particle radii between 0.35 and 0.7 μm) and "large" (particle
269 radii >0.7 μm) particles as well as the fraction of AOD due to "spherical" and
270 "nonspherical" particles at the four MISR spectral bands. Here, we compare the MISR
271 AOD at 550 nm from Version 22 of Level 2 with the model results.

272 **3.1.3 OMI**

273 OMI onboard the NASA Aura satellite has a daily global coverage, and crosses
274 the equator at 1:45 PM local time. The nadir horizontal resolution of OMI is 24×13 $km^2$.
275 In this study the OMAERUV Level 2 Collection 003 V1.4.2 product (Jethva et al., 2014)
276 is used as an independent data set providing SSA that is derived based on the reflectances
277 measured by the OMI instrument at 0.39 μm. The information on aerosol absorption in
278 OMI measurements comes, to a large extent, from the interaction with Rayleigh
279 scattering in the UV spectral region (Torres et al., 2013). The retrieved parameters are
280 also reported at 0.38 μm and 0.50 μm. Current OMI AOD has positive biases likely due
281 to a combination of factors including cloud contamination, surface albedo effects,

282 radiometric calibrations, and misidentified aerosol type (Ahn et al., 2008). Therefore, in
283 this study, OMI AAOD at 500 nm is reconstructed using the WRF-Chem simulated 500
284 nm AOD and OMI SSA at 500 nm with the formula of $AAOD_{OMI}=AOD_{MODEL}\times(1-SSA_{OMI})$.
285
286 **3.1.4 CALIPSO**
287 In this study, we use aerosol extinction profiles retrieved by the Cloud-Aerosol
288 Lidar with Orthogonal Polarization (CALIOP) onboard the Cloud-Aerosol Lidar and
289 Infrared Pathfinder Satellite Observation (CALIPSO) satellite. The CALIPSO satellite
290 was launched into a Sun-synchronous orbit on 28 April 2006. CALIOP is a dual-
291 wavelength polarization lidar and is designed to acquire vertical profiles of attenuated
292 backscatter from a near nadir-viewing geometry during both day and night phase (Winker
293 et al., 2007; Liu et al., 2004, 2008; Hu et al., 2007, 2009). In this study, the aerosol
294 extinction profiles at a nominal horizontal resolution of 5 km from the CALIPSO Level 2
295 profile products are used to evaluate the model. We focus on the CALIOP nighttime
296 observations in cloud-free condition, because nighttime observations have higher
297 accuracy than daytime observations (Winker et al., 2009).
298 The cloud-aerosol discrimination (CAD) score, which is an indicator that
299 measures confidence level of the discrimination between clouds (positive value) and
300 aerosols (negative value), is used to help screen out aerosol profiles that contain cloud
301 signals. We include the aerosol data with CAD score between -20 and -100, the same as
302 Yu et al., (2010, 2015). The other screening is to exclude aerosol layers where the
303 retrieval algorithm has to adjust the initially selected lidar ratio that is based on the type
304 and subtype of the aerosol layer to be analyzed. It should be noted that when the aerosol

extinction is not detected by CALIOP, we set its value and also the corresponding model result equal to zero, and then we compare CALIOP extinction profiles with the model and analyze the seasonal variation.

### 3.2 Ground-based observations

#### 3.2.1 AERONET

The AErosol RObotic NETwork (AERONET) is a globally distributed remote sensing network for aerosol monitoring from ground stations (Holben et al., 1998). AERONET uses the Cimel sun/sky photometer that measures AOD in 16 spectral channels (340-1640 nm). The measurements provide products every 15 minutes during daytime. In addition, an inversion algorithm is used for the retrieval of aerosol size distribution, complex refractive index, single-scattering albedo, and phase function (Dubovik and King, 2000; Dubovik et al., 2002). The spectral AOD from AERONET has an accuracy of ±0.01 (Eck et al., 1999; Holben et al., 2001). In the analysis presented in this paper, the cloud screened and quality assured level 2.0 products are used. AERONET products do not measure at wavelength 0.55 μm, so we calculate them through using the Angstrom exponent and the values at two nearest wavelengths 0.5 μm and 0.675 μm. The AERONET sites are located along the trans-Pacific transport pathways, so the products are important for evaluating the model results. Five sites over East Asia, one island site over the North Pacific, and four sites over the western U.S. are selected for comparison as shown in Figure 1.

#### 3.2.2 IMPROVE

The Interagency Monitoring for Protected Visual Environments (IMPROVE) network was initiated in 1985 by U.S. federal agencies including EPA, National Park

328 Services, Department of Agriculture-Forest Service, and other land management agencies
329 as a part of the EPA Regional Haze program (Malm et al., 1994). The network monitors
330 the visibility conditions and changes in national parks and wilderness areas on a long-
331 term basis. The detail sample collection and analytical methodology have been given by
332 Hand et al., (2011), and the data can be downloaded from
333 (http://views.cira.colostate.edu/fed/DataWizard/Default.aspx). There are 15 sites (Fig. 1)
334 along the west coast selected to compare with the surface aerosols of the model. In this
335 study, the mass concentrations of sulfate, nitrate, EC, OM, and dust in $PM_{2.5}$ (particulate
336 matter with aerodynamic diameter less than 2.5 μm) are used to evaluate the model. Most
337 IMPROVE data were directly downloaded, except for OM and dust. Because IMPROVE
338 reports only organic carbon (OC) measurements, in this study we multiply the OC data
339 by 1.4 for converting measured OC to OM (to account for hydrogen, oxygen, etc.) (Chow
340 et al., 2006; Zhao et al., 2013a). The fine dust is calculated following the formula (Malm
341 et al., 1994; Zhao et al., 2013a):

342 $$PM_{2.5}\text{-Dust} = 2.2[Al] + 2.49[Si] + 1.63[Ca] + 2.42[Fe] + 1.94[Ti]$$

343 Where [Al], [Si], [Ca], [Fe], and [Ti] represent the mass concentration of aluminum,
344 silicon, calcium, iron, and titanium, respectively.

345

346 # 4 Results

347 ## 4.1 Wind fields and precipitation

348 Winds and precipitation are two crucial meteorological factors playing important
349 roles in aerosol emission, transport, and removal. The seasonal mean wind fields at 850
350 hPa averaged for the period 2010-2014 from the WRF-Chem simulation are compared

351 with the Modern-Era Retrospective analysis for Research and Applications (MERRA)
352 reanalysis data (Rienecker et al., 2011) (Fig. 2). Strong westerly winds occur over the
353 North Pacific throughout the seasons with a peak (up to 12 m/s; 5.48 m/s on spatial
354 average) in boreal winter (DJF) followed by boreal spring (MAM) (4.46 m/s on spatial
355 average). The winds are weakest in boreal fall (SON) (4.1 m/s on spatial average). In
356 general, the model can well reproduce the spatial pattern of winds across the Pacific with
357 wind speeds of 4.1-5.41 m/s averaged spatially for the four seasons, with a spatial
358 correlation coefficient of 0.98 throughout the seasons. Figure 3 shows the spatial
359 distribution of seasonal mean precipitation from the Global Precipitation Climatology
360 Project (GPCP) observation (Huffman et al., 2001) averaged for the period 2010-2014
361 and the difference in the WRF-Chem simulation. Over East Asia, precipitation reaches a
362 maximum during the boreal summer (JJA) followed by MAM. In the North Pacific basin,
363 the largest precipitation occurs in DJF along the storm tracks with the maximum
364 westerlies. Over the U.S. west coast, precipitation peaks during DJF and reaches a
365 minimum in JJA. The simulation reasonably reproduces the spatial and seasonal
366 variations of precipitation with spatial correlation coefficients of 0.89, 0.81, 0.81, and
367 0.84 for DJF, MAM, JJA, and SON, respectively. The simulation overestimates annual
368 mean precipitation averaged over the North Pacific (3.1 mm $day^{-1}$ and 4.2 mm $day^{-1}$,
369 respectively, from GPCP and WRF-Chem). The overestimation (more than 50%) is
370 particularly over the Inter-Tropical Convergence Zone (ITCZ) and the western tropical
371 Pacific that are south to the 20°N and the major pathway of trans-Pacific transport. The
372 excessive precipitation over the tropical Pacific may be due to biases from the convective
373 parameterizations in producing tropical precipitation in WRF, such as overestimation of

374 precipitation efficiency from the simple treatment of cloud microphysical processes in
375 convective clouds, and biases in the prescribed temperature and humidity reference
376 profiles (e.g., Fonseca et al., 2015; Hagos et al., 2016). Short sensitivity experiments we
377 performed show that the WRF simulated tropical precipitation is sensitive to the choice
378 of convective parameterizations (not shown).
379
380 **4.2 Aerosol optical depth**
381 4.2.1 Spatial and temporal variation
382 Figure 4 shows the spatial distributions of seasonal mean AOD at 550 nm across
383 the Pacific from Asia to North America averaged for 2010-2014 from the retrievals of
384 MODIS and MISR onboard Terra and the corresponding WRF-Chem simulation. The
385 WRF-Chem simulated AOD at 600 nm and 400 nm are used to derive the AOD at 550
386 nm (using the Angström exponent). In order to reduce the sampling discrepancy between
387 the two retrievals, the daily results from the two satellite retrievals and simulation are
388 sampled and averaged at the same time and location. This way of averaging leads to the
389 blank areas of missing values, which are relatively large in JJA. Satellite retrievals show
390 consistent spatial pattern with the spatial correlation coefficients of 0.65-0.88 for the four
391 seasons. The MODIS retrieval shows higher AOD over the semi-arid regions (e.g.,
392 Northwest China and the southwestern U.S.) than the MISR retrieval; however the
393 MODIS retrieved AOD magnitude over these regions is significantly overestimated
394 because of its large uncertainties in the assumed surface reflectance in semi-arid regions
395 (Remer et al., 2005; Levy et al., 2013). In comparison, the MISR observations in the
396 western U.S. show better quality presumably because of the multi-angle capability that

allows for a better characterization of surface reflectance. Both retrievals indicate that AOD is high over the Asian continent and gradually decreases across the Pacific. High AOD coincides with the sub-tropical jet (30°N-50°N, Fig. 2) over the Pacific and results from wind-induced increase in sea-salt loading and the Asian pollutant outflow. Seasonal variation of aerosols across the Pacific is evident, with peak AOD over the western Pacific in MAM and minimum AOD in JJA and SON. This seasonal variation is generally consistent with previous studies (Yu et al., 2008, 2012), although our sampling method results in more missing data from satellite retrievals in JJA than other seasons. Previous studies found that trans-Pacific transport of air pollutants is most efficient in MAM due to active cyclonic activity and that pollutants are lifted to the free troposphere where they can be rapidly transported across the Pacific by strong westerlies (e.g., Forster et al., 2004; Liang et al., 2004; Heald et al., 2006; Yu et al., 2008).

The WRF-Chem simulation generally well captures the observed spatial and seasonal variability of AOD across the Pacific with the spatial correlation coefficients of 0.63-0.76 for the four seasons against the MISR retrievals. The model generally underestimates the retrieved AOD over the North Pacific (0°-60°N, 120°E-120°W) with an annual mean value of 0.11, which is lower than the retrieved values of 0.14 (MODIS) and 0.15 (MISR). Over the region north of 20°N (20°N-60°N, 120°E-120°W), the simulation produces an average AOD of 0.14 that is more consistent with the retrieved values of 0.15 (MODIS) and 0.16 (MISR). This negative bias of the oceanic AOD south of 20°N may be due to underestimation of marine emissions (Yu et al., 2003) and/or overestimation of aerosol wet removal associated with the positive bias in precipitation (Fig. 3). The discrepancy may also be due to the higher uncertainty at low aerosol level

(Levy et al., 2013) and cloud contamination in the retrievals that leads to an overestimation of AOD in some regions of the North Pacific (e.g., Zhang and Reid, 2006). The model also simulates lower AOD over the continent of North America compared with satellite retrievals. The difference between the simulation and retrievals may be due to the uncertainty in satellite retrievals over the continents (e.g., Liu et al., 2004; Levy et al., 2010).

Since this study focuses on the trans-Pacific transport and evolution of aerosols, the Pacific is further divided into three sub-regions (Region 1: 20°N-50°N and 120°E-140°E; Region 2: 20°N-50°N and 140°E-140°W; Region 3: 20°N-50°N and 140°W-120°W) representing the West Pacific, the Central Pacific, and the East Pacific shown as the black boxes in Figure 4 for analysis. Figure 5 shows the seasonal mean 550 nm AOD over the three sub-regions from the MISR and MODIS retrievals and the corresponding WRF-Chem simulation at the pass time of MISR and MODIS, respectively, averaged for 2010-2014. The retrievals show clearly that AOD peaks in MAM followed by DJF in all the regions across the Pacific. The simulated annual mean AOD of 0.21, 0.16, and 0.09 over the West, Central, and East Pacific, respectively, successfully reproduce the observed values of 0.22, 0.16, and 0.10 from MODIS and 0.21, 0.16, and 0.10 from MISR. The simulation also captures the seasonal variability with the maximum AOD in MAM followed by DJF. In general, the MODIS and MISR retrievals and simulation consistently show that AOD reduces from the West Pacific to the East Pacific. The interannual variability of AOD over the three sub-regions is small for 2010-2014 indicated by the retrievals and simulation (not shown).

442 Available observations from several AERONET sites (Fig. 1) over East Asia, the
443 Pacific, and the western U.S. are also compared with the model simulation. Figure 6
444 shows the comparison of observed and simulated AOD at three representative
445 AERONET sites for 2010-2014 over East Asia, an island of the Pacific, and the western
446 U.S. coast. The observations and simulation agree well at all three sites, and both reflect
447 the AOD gradient from East Asia to the western U.S. as shown in Figure 4. Observed
448 AOD is the highest with a mean value of 0.31 at the SACOL site over East Asia and
449 reduces to 0.075 at the Midway_Island site, and 0.045 at the Frenchman_Flat site. The
450 model reproduces exactly these values at the three sites with correlation coefficients of
451 0.45, 0.65, and 0.64, respectively. About 90% of simulated AOD is within a factor of 2 of
452 the AERONET measurements.
453 Figure 7 further shows the monthly variation of AOD averaged at the AERONET
454 sites over East Asia, the Pacific island, and the West U.S. (as shown in Fig. 1) from the
455 AERONET observations, MODIS and MISR retrievals, and WRF-Chem simulation. For
456 the simulated AOD, contributions by dust, BC, OM, sulfate, and other aerosols are also
457 shown. Over East Asia, the MISR and AERONET retrievals agree well with the annual
458 mean of 0.37 and 0.33, respectively. Their monthly variation correlates with a coefficient
459 of 0.8. The MODIS retrievals with the annual mean of 0.48 generally overestimate AOD
460 against the AERONET retrievals and correlate with the AEROENT retrieved monthly
461 AOD with a coefficient of 0.67. The simulation reproduces the AERONET observed
462 AOD variability with an annual mean of 0.38 and a monthly correlation coefficient of
463 0.74. Model results show that anthropogenic aerosols dominate the AOD from summer to
464 winter while dust can significantly contribute to the AOD in spring. Over the island of

Pacific (the Midway_Island site), retrievals from AERONET, MODIS, and MISR are generally consistent with each other on annual mean with values of 0.14, 0.13, and 0.14, respectively. The MISR retrievals correlate well with the AERONET retrievals in monthly variation with a coefficient of 0.70, which is 0.42 for MODIS, showing a minimum in summer months. The simulated annual mean AOD of 0.14 well reproduces the AERONET retrieval. The model also captures the AERONET retrieved monthly variation of AOD with a correlation coefficient of 0.64. The simulation shows that this monthly variation is largely determined by the variation of sea-salt aerosol (e.g., Smirnov et al., 2003) and Asian pollutant outflow. The trans-Pacific transported aerosols (other than sea-salt) show strong monthly variation with a maximum in April and a minimum in July. Over the western U.S., the MISR and MODIS retrievals well capture the monthly variation of AERONET retrievals with correlation coefficients of ~0.9, but MISR and MODIS retrieve an annual mean AOD of 0.12 and 0.20, respectively, which are higher than the AERONET retrieval of 0.07, particularly in March-October. The simulated annual mean AOD of 0.07 reproduces the AERONET retrieval. The simulation also correlates well with the AERONET retrievals with a coefficient of 0.76 in monthly variation. Both the AERONET retrieval and simulation show that the largest AOD occurs in the spring months, which has significant contribution from the dust aerosol transported across the Pacific (to be discussed in Section 4.5). The simulation compares more consistently with the AERONET retrieval than with the MISR and MODIS retrievals in terms of magnitude, which suggests that the difference between the MODIS and MISR retrievals and the simulation over the western U.S. shown in Figure 4 is largely due to uncertainties associated with the satellite retrievals. The simulation underestimates the

AERONET retrieved AOD in July-September. This underestimation may come from the model significant negative biases in carbonaceous aerosols in the warm season (to be discussed in Section 4.5).

4.2.2 Wavelength dependence

The wavelength dependence of AOD that can be represented by the extinction Angstrom exponent (EAE) is an indicator of aerosol particle size (Angstrom, 1929; Schuster et al., 2006). In general, relatively small values of EAE indicate that aerosol size distributions are dominated by coarse aerosols typically associated with dust and sea-salt, while relatively large values of EAE indicate fine aerosols usually contributed by anthropogenic pollution and biomass burning. Figure 8 shows the seasonal mean EAE averaged for 2010-2014 from the MODIS retrievals and the WRF-Chem simulation over the three sub-regions. The retrievals show clearly that the seasonal median EAE values peak at 1.25, 0.74, and 0.89 in JJA and reach a minimum of 0.68, 0.20, and 0.21 in DJF in three sub-regions of the West, Central, and East Pacific, respectively. This seasonality reflects the fact that photochemistry is most active in JJA to produce fine aerosol particles such as sulfate. In general, the simulation successfully reproduces the observed EAE seasonality with the JJA maximum of 1.09, 0.82, and 0.79 and the DJF minimum of 0.83, 0.42, and 0.35 in the three sub-regions, respectively. The retrievals and simulation also show that the values of EAE are greater in the West Pacific than in the Central and East Pacific. This pattern may reflect the dominance of the Asian pollutant outflow on the aerosol size distributions over the West Pacific, while the relatively large-size particles of

510 sea-salt dominates in the other two regions. Again, the annual variability of EAE over the
511 three sub-regions is small (not shown).
512
513 **4.3 Aerosol absorption optical depth**
514 Light absorbing aerosols such as BC and dust play an important role in the
515 atmosphere to absorb radiation and change the heating profiles in the atmosphere.
516 Aerosol absorption optical depth (AAOD) is an important parameter for evaluating the
517 model performance in simulating light absorbing aerosols. Figure 9 shows the seasonal
518 mean AAOD at 500 nm averaged for 2010-2014 and over the three sub-regions from the
519 OMI retrieval and the WRF-Chem simulation. The model simulated AAOD at 600 nm
520 and 400 nm are used to derive the AAOD at 500 nm (using the Angström exponent).
521 Both retrievals and simulation show small interannual variability (not shown). The
522 simulated seasonal mean AAOD of 0.015 over the West Pacific agrees reasonably well
523 with the OMI retrieval of 0.014 in DJF but is higher in the other three seasons, with the
524 largest difference in JJA. The significantly lower AAOD in seasons other than DJF from
525 the OMI retrieval is also shown in the comparison with the AERONET retrieval (to be
526 discussed with Fig. 10). Over the Central Pacific, the simulated seasonal mean AAOD of
527 0.014 and 0.006 in MAM and SON, respectively, generally reproduces the retrieved
528 AAOD of 0.017 and 0.005, but the model overestimates (underestimates) the retrieved
529 values in JJA (DJF) with 0.008 (0.005) from the simulation and 0.004 (0.009) from the
530 retrieval. This difference may reflect the model deficiency in simulating Asian BC
531 outflow over the Pacific in JJA and DJF, but may also result from retrieval uncertainties.
532 The OMI retrievals may have difficulty in distinguishing the ocean color effects from

533 those of low aerosol concentrations in the UV spectral range and ignoring the less-
534 sufficient amounts of absorbing aerosols (Veihelmann et al., 2007; Torres et al., 2013).
535 Jethva et al. (2014) found that the most important source of uncertainty in OMI AAOD is
536 the effect of sub-pixel cloud contamination related to the sensor's coarse spatial
537 resolution, which causes AAOD underestimations for cases of low aerosol load. Over the
538 East Pacific, the simulated seasonal mean AAOD of 0.0035, 0.0091, 0.0048, and 0.0042
539 for DJF, MAM, JJA, and SON, respectively, are generally consistent with the retrieved
540 values of 0.005, 0.007, 0.0012, and 0.003, which shows the maximum value in MAM.
541 The most significant difference occurs in JJA. Similar as over the Central Pacific, the
542 underestimation of retrieved AAOD over the clean region may contribute to the
543 difference. The retrievals and simulation show large variability of AAOD, and they
544 generally agree within the 10th and 90th percentiles of each other. AAOD is larger over
545 the West Pacific than the Central and East Pacific, which is consistent with the AOD
546 pattern. The simulation shows that AAOD peaks in MAM followed by JJA over the three
547 sub-regions, which may be due to the stronger outflow of dust and anthropogenic
548 pollutants in the two seasons.

549 The AERONET retrieval products (version 2) also provide AAOD values but
550 only at the sites and time when the total AOD exceeds a threshold value of 0.4 at 440 nm
551 because the AERONET inversion algorithms require a high signal-to-noise ratio to
552 retrieve some optical products such as AAOD. The total AOD values over the Central
553 Pacific and the western U.S. are less than this threshold value most of the time, and only
554 AAOD values retrieved at the East Asian sites are available and reliable. Figure 10 shows
555 the monthly variation of AAOD averaged at the AERONET sites over East Asia (Fig. 1)

556 from the AERONET observation, OMI retrieval, and WRF-Chem simulation. The
557 AERONET retrieval shows the monthly variation of AAOD over East Asia with
558 relatively lower values in JJA probably due to wet removal of aerosols by precipitation
559 and mixing with clean marine air during the East Asian summer monsoon (Zhao et al.,
560 2010). The simulation generally captures the observed monthly variability with the
561 minimum AAOD of 0.035 and 0.032 in July from the simulation and the AERONET
562 retrieval, respectively, and the maximum of 0.055 and 0.054 in October, respectively.
563 The model overestimates AAOD in the warm months (May-September) with the mean
564 values of 0.046 and 0.036 from the simulation and retrieval, respectively, and
565 underestimates AAOD in December and January with the mean values of 0.037 and
566 0.043, respectively. The model positive (negative) biases in AAOD in the warm (cold)
567 months may be partly related to the constant anthropogenic BC emissions applied
568 throughout the seasons, but previous studies have shown that anthropogenic BC
569 emissions over China may have seasonal variation, with roughly 6% versus 13% of the
570 annual total BC emission in summer and winter, respectively, estimated in Lu et al.
571 (2011). The simulation shows that AAOD over East Asia is dominated by BC and is
572 partly contributed by dust. Other aerosols contribute to small amount of AAOD due to
573 the internal mixing of aerosols in the atmosphere (Zhao et al., 2013a). The OMI retrieved
574 AAOD is lower than that from AERONET and WRF-Chem, particularly in JJA and SON.
575 The lower OMI AAOD over East Asia may also indicate its negative biases over the
576 West Pacific (Fig. 9) where the air is significantly affected by the East Asian outflow.
577 The biases in the OMI algorithm of retrieving SSA over East Asia may be also applied
578 over the West Pacific.

579

580 **4.4 Aerosol vertical distributions**

581 Column integrated properties of aerosol (e.g., AOD and AAOD) provide useful
582 information in regard to atmospheric aerosol loading but little information on the vertical
583 distribution of aerosols. Previous studies have found that simulated aerosol vertical
584 distributions differ significantly, which can affect the assessments of aerosol impacts on
585 climate and air quality (e.g., Schulz et al., 2006; Textor et al., 2006). CALIPSO with the
586 unique capability provides an opportunity to assess model simulation of aerosol vertical
587 distributions (e.g., Huang et al., 2013). Figure 11 shows the vertical distributions of
588 annual mean aerosol extinction coefficients for 2010-2014 averaged over the three sub-
589 regions from the CALIPSO retrieval and the corresponding WRF-Chem simulation under
590 cloud-free condition. The model results are sampled for averaging at the locations and
591 times where and when retrievals are available. The CALIPSO retrieval shows clearly that
592 aerosol extinction coefficients peak near several hundred meters above the surface and
593 then decrease with the altitude over the three sub-regions. The extinction coefficients
594 reduce from the West to East Pacific. The model generally reproduces the aerosol
595 extinction vertical variation with correlation coefficients of 0.95-0.97. The simulated
596 aerosol extinction coefficients are consistent with the retrievals around 0.5-1 km with
597 difference within 15%. The difference increases in the free troposphere and below 0.5 km.
598 The simulation is higher than the retrieval in the free troposphere (e.g., about a factor of 2
599 around 4 km), which may be due to the reduced sensitivity of CALIPSO to tenuous
600 aerosol layers above 4 km (Yu et al., 2010). The lower (up to 30% lower) simulated
601 extinction coefficients below 0.5 km in all three sub-regions may indicate negative biases

602 in estimating marine aerosol emissions and excessive wet scavenging of the model, as
603 shown in Fig. 4. The in-situ measurements over the region are needed for further
604 validating both remote sensing data and the simulation. The simulated mass fraction of
605 each aerosol component (Fig. 12) shows that below 1 km, sea-salt dominates the total
606 aerosol mass over the Central and East Pacific, while the outflow of anthropogenic
607 aerosols and dust also makes significant contributions over the West Pacific. Above 4 km,
608 dust is the dominant aerosol over all three sub-regions.

609 The seasonal variation of aerosol extinction profiles averaged for 2010-2014 (Fig.
610 13) shows the spring maximum, particularly above 2 km, over all three sub-regions from
611 both the CALIPSO retrievals and the model simulation. This is likely due to the
612 seasonality of dust outflow over the Pacific (Fig. 14) that dominates the aerosol masses
613 above 2 km with a peak in spring (e.g., Huang et al. 2013). The model reasonably
614 reproduces the retrieved aerosol extinction vertical variation through the seasons over the
615 three sub-regions with the correlation coefficients of 0.93-0.98. Over the West Pacific,
616 the simulation has larger negative biases (up to 35%) below 1 km in DJF when sea-salt
617 has a relatively larger contribution near the surface (Fig. 14) than other seasons (up to 15-
618 25%), and has positive biases above 1 km. At 1-4 km, the simulated aerosol extinction is
619 higher (up to a factor of 2) than the retrieval and the difference increases with the altitude.
620 The comparison between the simulation and retrieval at 1-4 km is the best in DJF with
621 the difference within 15%. In JJA, the aerosol mass has the largest contribution from the
622 anthropogenic pollutant outflow among the seasons with a peak at ~ 2 km above the
623 surface. Over the Central and East Pacific, the model has smaller negative biases (up to
624 20%) below 1 km than over the West Pacific and the maximum negative bias is in DJF.

625 Over these two regions, the seasonality of the vertical shape of each aerosol component
626 contribution is similar to that over the West Pacific, except that the sea-salt contribution
627 is larger near the surface (Fig. 14).
628
629 **4.5 Aerosol surface mass concentrations over the West U.S.**
630 For lack of in-situ observations of aerosol masses over the Pacific, measurements
631 of surface fine aerosol ($PM_{2.5}$) component mass concentrations from the IMPROVE
632 network over the western U.S. were widely used for model evaluation of trans-Pacific
633 transport (e.g., Chin et al., 2007; Hadley et al., 2007). Daily variation of surface fine
634 aerosols (dust, sulfate, nitrate, BC, and OM) averaged for 2010-2014 from the IMPROVE
635 measurements and the monthly mean of measurements and corresponding model
636 simulation are illustrated in Figure 15. The IMPROVE sites over the western U.S. (Fig. 1)
637 that have measurements for the entire five years (2010-2014) and with less noisy values
638 are divided at 40°N into two groups to represent the Northwest and Southwest U.S. The
639 averaged values over the Northwest and Southwest sites are shown.
640 At both Northwest and Southwest sites, the model generally captures the observed
641 monthly variation of dust with the correlation coefficients of 0.61 and 0.55, respectively.
642 Both the observation and simulation show the maximum dust mass concentration in
643 MAM and the minimum in DJF. The model simulates higher annual mean surface dust
644 concentrations (0.25 μg $m^{-3}$ and 0.56 μg $m^{-3}$ over the Northwest and Southwest,
645 respectively) than the observation (0.18 μg $m^{-3}$ and 0.35 μg $m^{-3}$, respectively). The
646 observed surface sulfate concentrations are the lowest in the cold season (0.17 μg $m^{-3}$ and
647 0.18 μg $m^{-3}$ in DJF over the Northwest and Southwest, respectively) when

photochemistry is least active, and the highest in the warm season (0.47 μg $m^{-3}$ and 0.63 μg $m^{-3}$ in June-September, respectively) when the most active photochemistry occurs. This seasonality of sulfate may also be contributed by the seasonality of wet removal (much more precipitation in DJF). Over the Northwest and Southwest, the simulation generally reproduces the magnitude and seasonality of sulfate with the minimum surface concentrations of 0.17 μg $m^{-3}$ and 0.25 μg $m^{-3}$, respectively, in DJF and the maximum surface concentrations of 0.49 μg $m^{-3}$ and 0.62 μg $m^{-3}$, respectively, in June-September, and monthly correlation coefficients of 0.78 and 0.83, respectively. Nitrate shows a seasonality that is opposite to that of sulfate, with a maximum surface concentration occurring in the cold season (0.72 μg $m^{-3}$ and 1.22 μg $m^{-3}$ in DJ over the Northwest and Southwest, respectively) and a minimum in the warm season (0.25 μg $m^{-3}$ and 0.35 μg $m^{-3}$ in JJA, respectively), which can be explained by the combined effects of temperature and vertical turbulent mixing (Zhao et al., 2013a). The simulation generally reproduces the seasonality of nitrate with a monthly correlation coefficient of 0.75 and 0.83 over the Northwest and Southwest, respectively. Over the Northwest and Southwest, the model simulates reasonably the maximum surface nitrate concentration of 0.69 μg $m^{-3}$ and 1.35 μg $m^{-3}$, respectively, in the cold season and the minimum with values of 0.18 μg $m^{-3}$ and 0.42 μg $m^{-3}$, respectively, in the warm season. The simulation has relatively larger positive biases (a factor of 2) in months (February, March, October, and November) between the cold and warm seasons, which may reflect the model deficiency in aerosol thermodynamics (i.e., the partitioning of nitrate aerosol to the gas phase in these months is too slow in the model). In general, both observation and simulation show higher surface dust, sulfate, and nitrate concentrations over the Southwest than the Northwest.

671 A sensitivity simulation without dust, fire, and anthropogenic emissions over
672 North America (10°N-70°N and 170°W-60°W) indicates that the trans-Pacific
673 transported dust dominates the total dust amount in all seasons at the northern and
674 southern sites with the contribution of 80% and 60%, respectively, on annual mean,
675 particularly in MAM with the contribution of >90% and ~85%, respectively. At the
676 southern sites, the trans-Pacific dust makes the lowest contribution of 19% in DJF. The
677 large contribution of trans-Pacific dust indicates that the simulated overestimation of
678 surface dust concentrations may be resulted from the excessive trans-Pacific transport of
679 dust, which is also indicated in the comparison with the CALIPSO retrieval that shows
680 the simulated aerosol extinction is overestimated above 1 km over the North Pacific. The
681 difference may also be partly from the observation uncertainties. As described in Section
682 3.2.2, the mass of soil dust is calculated from a linear combination of the measured
683 elements associated predominantly with soil, including Al, Si, Ca, Fe, and Ti. The
684 uncertainties associated with the reported dust values reflect the range and variation of
685 mineral composition from a variety of soil types. The sensitivity simulation also shows
686 that trans-Pacific transported sulfate can make significant contribution to its surface
687 concentration over the western U.S., and the relative contributions are larger when the
688 surface concentrations are lower with ~60% in DJF averaged at all sites and ~35% in JJA.
689 The trans-Pacific nitrate contributes a relatively small amount (~15%) to the total nitrate
690 surface concentration.

691 There is a significant difference in BC and OM surface concentrations between
692 the observations and simulation. At the Northwest sites, the observed BC and OM show
693 significant seasonal variation with the highest surface concentration in June-September

694 (JJAS). The sensitivity simulation shows that the peak is dominated by the North
695 American emission that is contributed by biomass burning with a maximum in JJAS
696 (Chin et al., 2007). The simulation captures this seasonality to some extent with monthly
697 correlation coefficients of 0.74 and 0.69 for BC and OM, respectively. However, the
698 simulation significantly underestimates the JJAS peak with 0.05 μg $m^{-3}$ and 0.49 μg $m^{-3}$
699 BC and 0.5 μg $m^{-3}$ and 4.5 μg $m^{-3}$ OM from the simulation and observation, respectively.
700 These significant negative biases in the model are likely from uncertainties in the
701 GFEDv3 biomass burning inventory for the simulation period. The monthly mean
702 emissions at a relatively coarse horizontal resolution may not be able to capture the
703 strong local fire events. Mao et al. (2011) pointed out that the GFED inventory may
704 underestimate the magnitude of biomass burning emissions in the western U.S. due to the
705 issue of detecting small fires, for example, from prescribed and agricultural burning (e.g.,
706 Randerson et al., 2012; Giglio et al., 2010). Mao et al. (2014) estimated that the biomass
707 burning BC emissions inverted from the IMPROVE observations can be a factor of 5
708 higher than the GFED inventory in July-September over the Western U.S. Another
709 biomass burning emission inventory FINN (Fire INventory from Ncar) (Wiedinmyer et
710 al., 2011) also shows a factor of 3 higher BC emissions than the GFED inventory over the
711 Northwest U.S. (100°W-125°W and 40°N-50°N) in September 2011 (not shown).
712 At the Southwest sites, the impact of biomass burning on the BC and OM surface
713 concentrations seems relatively small. The observations show the maximum BC surface
714 concentration of 0.17 μg $m^{-3}$ in DJF and the minimum of 0.09 μg $m^{-3}$ in JJA, which is
715 likely due to stronger vertical turbulent mixing in JJA compared with DJF (Zhao et al.,
716 2013a). The simulation can well capture the magnitude and seasonality of surface BC

717 concentration with the monthly correlation coefficient of 0.78 and the maximum of 0.19
718 μg $m^{-3}$ in DJF and the minimum of 0.10 μg $m^{-3}$ in JJA. The observed OM still shows the
719 peak concentration of 1.27 μg $m^{-3}$ in JJA, and the model significantly underestimates the
720 peak OM concentration with a value of 0.20 μg $m^{-3}$. The negative bias of OM over the
721 Southwest seems not to be related to the underestimation of biomass burning because BC
722 is reasonably simulated. This seasonal variability may be determined by the secondary
723 production of OM, which peaks in JJA because photochemistry is more active and
724 emissions of biogenic volatile organic compounds are higher in the warm season. The
725 underestimation of secondary organic aerosol (SOA) may be due to the uncertainty of
726 biogenic emissions (Zhao et al., 2016) and the outdated SOA mechanism used in the
727 current version of WRF-Chem (Shrivastava et al., 2011). Besides the emission and model
728 deficiency, another source of the difference between the simulation and observation may
729 be from the sub-grid variability of emissions and surface concentrations that confounds
730 the comparison of model simulation at one-degree horizontal grid resolution and the point
731 measurements from the individual sites. On the other hand, it is also noteworthy that
732 uncertainties in the IMPROVE carbonaceous aerosol data are also relatively high because
733 they are inferred from optical/thermal measurements. The sensitivity simulation again
734 shows that the peaks of BC and OM surface concentrations are dominated by the North
735 American emissions.
736

737 ## 5 Summary and conclusion

738 A fully coupled meteorology-chemistry model (WRF-Chem) has been configured
739 to conduct quasi-global simulation for the 5 years of 2010-2014. The simulation results

740 are evaluated for the first time with various reanalysis and observational datasets,
741 including precipitation from GPCP, wind fields from MERRA, AOD, EAE, and AAOD
742 from MODIS, MISR, OMI, and AERONET, aerosol extinction profiles from CALIPSO,
743 and aerosol surface mass concentrations from IMPROVE. In this study, the evaluation
744 and analysis focus on the trans-Pacific transport region for the purpose of demonstrating
745 the capability of using the quasi-global WRF-Chem simulation to provide consistent
746 lateral chemical boundaries for nested regional WRF-Chem simulations that can be used
747 to investigate the impact of trans-Pacific transported aerosols on the regional air quality
748 and climate over the western U.S. The main conclusion is summarized below:

749 ▪ The comparison of simulated AOD with the satellite and AERONET retrievals
750 reveals that the model can well capture the spatial gradient of aerosol mass loading
751 decreasing from the West to East Pacific, resulting from the sea-salt loading and the
752 Asian pollutant outflow. The seasonal variation of aerosols across the Pacific with the
753 maximum AOD in MAM is also reproduced by the model. The model underestimates
754 AOD over the ocean to the south of 20°N and over the continent of North America
755 against the satellite retrievals. This discrepancy may reflect the model
756 underestimation of marine emissions and/or overestimation of aerosol wet removal or
757 the positive retrieval errors due to cloud-contamination. Compared with the
758 AERONET retrieval, the difference of AOD over the western U.S. between the
759 simulation and satellite retrievals may be due to the uncertainty in the satellite
760 retrievals over the continent.

761 ▪ The assessment of simulated EAE indicates that the model generally captures the
762 observed smaller-size aerosols over the West Pacific contributed by the Asian

763 pollutant outflow compared to the relatively larger particles over the Central and East
764 Pacific with more contributions from sea-salt. The model also simulates the consistent
765 seasonality of EAE with observations showing a minimum in DJF and a maximum in
766 JJA due to the active production of small particles in warm seasons.
767 ▪ The model reasonably simulates the decreasing gradient of OMI derived AAOD from
768 the East to West of Pacific. The simulation shows a peak of AAOD in MAM due to
769 the strong outflow of dust and anthropogenic pollutants. The comparison with
770 AERONET retrieved AAOD over East Asia may indicate that the OMI SSA retrieval
771 has positive biases over East Asia and also the West Pacific, particularly in JJA. Over
772 East Asia, the model positive (negative) biases in AAOD in the warm (cold) months
773 may be partly due to the neglect of the seasonal variability of anthropogenic BC
774 emissions in this study.
775 ▪ The model generally captures the CALIPSO retrieved vertical gradient of aerosol
776 extinction coefficients roughly decreasing with the altitude over the Pacific. Near the
777 surface, the model biases in estimating marine aerosol emissions may contribute to
778 the discrepancy between the simulation and retrievals. The difference between the
779 simulation and retrievals in the free troposphere may be due to the reduced sensitivity
780 of CALIPSO to the aerosol layers above 4 km. The model well captures the
781 seasonality of aerosol extinction profiles with a maximum in MAM, which is largely
782 controlled by the activity of dust outflow events over the Pacific.
783 ▪ Compared with the measurements from the IMPROVE sites over the western U.S.,
784 the model simulates reasonable magnitudes and seasonality of the observed sulfate
785 and nitrate surface concentrations with peaks in JJA and DJF, respectively. The

simulation has relatively larger positive biases of nitrate surface concentrations in early spring and late fall, which may reflect the model deficiency in aerosol thermodynamics that the partitioning of nitrate aerosol to the gas phase in these months is too slow in the model. The simulation captures the observed seasonality of dust surface concentrations with the maximum and minimum in MAM and DJF, respectively, but generally overestimates the observed dust surface concentrations, which may be due to the excessive trans-Pacific dust. The difference may also be partly from the observation uncertainties. Over the southwestern U.S., the simulation reproduces the magnitude and seasonality of surface BC concentrations that show the maximum in DJF, but significant underestimates the surface OM concentrations in JJA likely due to the negative biases in SOA production. Over the northwestern U.S., the simulation significantly underestimates surface BC and OM concentrations likely due to the uncertainties in fire emissions that may not capture the strong local fire events. Another source of the difference may be due to the discrepancy in spatial scales between site observations and model outputs for the grid cell area of one-degree resolution. In addition, uncertainties in IMPROVE may also contribute to the discrepancy, in particular for carbonaceous aerosols that are inferred from optical/thermal measurements.

- The sensitivity simulation shows that the trans-Pacific transported dust dominates the dust surface concentrations in the western U.S., particularly in MAM. The trans-Pacific transported sulfate and nitrate can also make significant contribution to their surface concentrations over the rural areas of the western U.S. The peaks of BC and OM surface concentrations over the western U.S. are dominated by the North

809 American emissions. These sensitivity simulation results may be different to some
810 extent from other models (e.g., Chin et al., 2007), which could result from the
811 considerable differences in aerosol composition and vertical distributions due to
812 differences in model treatments of emissions and removal processes as revealed by
813 several inter-comparison studies (Barrie et al., 2001; Penner et al., 2002; Textor et al.,
814 2006). More detailed model inter-comparison of the trans-Pacific transport of
815 aerosols deserves further study.

816 Although dust and biomass burning emissions in general have considerable year-
817 to-year variations, the interannual variability of seasonal AOD for 2010-2014 averaged
818 over the three sub-regions of the Pacific is small as indicated by the retrievals and
819 simulation. It is noteworthy that the trans-Pacific aerosols identified in this study include
820 not only the outflow of Asian pollutants and dust but also European pollutants and
821 African dust that are transported to Asia and then merged with the Asian outflow. This
822 has been recognized by previous studies (e.g., Chin et al., 2007). The evaluation in this
823 study successfully demonstrates that the WRF-Chem quasi-global simulation with some
824 improvements in emission inventories can be used for studying trans-Pacific transport of
825 aerosols and providing reasonable inflow chemical boundaries for the western U.S. to
826 further understand the impact of transported pollutants on the air quality and regional
827 climate with high resolution nested regional modeling. It needs to be noted that the
828 aerosol optical properties, such as AOD, AAOD, and EAE, derived from the retrievals
829 and simulation have some different assumptions of the physical and optical parameters,
830 so that the link between the model and the satellite data are only qualitative or semi-
831 quantitative. Evaluation of model results with in-situ observations would be informative.

In-situ data even for specific events are valuable especially over Asia and the Pacific where public data are currently sparse or inaccessible, although some observations may be obtained through collaborations. Last but not least, the model biases against observations may be also partly contributed by the uncertainties in emissions. Some recently updated anthropogenic emissions (e.g., Janssens-Maenhout et al., 2015; Li et al., 2016) and other biomass burning emissions with higher temporal and spatial resolutions (e.g., Wiedinmyer et al., 2011) may be used in future studies to investigate the impact of emission uncertainties on trans-Pacific aerosols over the West U.S.

## Code availability

The WRF-Chem version 3.5.1 release can be obtained at http://www2.mmm.ucar.edu/wrf/users/download/get_source.html. A general WRF-Chem user's guide is also available online (http://ruc.noaa.gov/wrf/WG11/). Code modifications include changes to the chemical boundary treatment using periodic boundary conditions in the zonal direction for quasi-global WRF-Chem simulation. Other changes to the model include the oceanic (sea salt and dimethyl sulfide) emission schemes and the convective transport and removal scheme of tracers that play a significant role in quasi-global WRF-Chem simulations of aerosols. These modifications and model configuration for conducting quasi-global WRF-Chem simulations here are available upon request by contacting the corresponding author and will be incorporated in the future available release of WRF-Chem.

## Acknowledgements

855 This research was supported by the Office of Science of the U.S. Department of Energy
856 (DOE) as part of the Regional & Global Climate Modeling (RGCM) program. J. Huang
857 acknowledges support from the National Basic Research Program of China
858 (2012CB955301). H. Yu was supported by NASA CALIPSO project (NNX14AB21G)
859 managed by Dr. David Considine. This study used computing resources from the PNNL
860 Institutional Computing. Pacific Northwest National Laboratory is operated by Battelle
861 Memorial Institute for the DOE under contract DE-AC05-76RL01830. The CALIPSO
862 data were obtained from the NASA Langley Research Center Atmospheric Sciences Data
863 Center. MODIS and MISR data were obtained from the NASA Atmospheric Science
864 Data Center. OMI data were obtained from the NASA Goddard Earth Sciences Data and
865 Information Services Center.
866
867

## Reference


Ahn, C., O. Torres, and P. K. Bhartia: Comparison of Ozone Monitoring Instrument UV Aerosol Products with Aqua/Moderate Resolution Imaging Spectroradiometer and Multiangle Imaging Spectroradiometer observations in 2006, 113, D16S27, doi:10.1029/2007JD008832, 2008.

Alizadeh-Choobari, O., P. Zawar-Reza, and A. Sturman: The global distribution of mineral dust and its impacts on the climate system: A review, Atmospheric Research 138, 152–165, doi:10.1016/j.atmosres.2013.11.007, 2014.

Alizadeh-Choobari, O., A. P. Sturman, and P. Zawar-Reza: Global distribution of mineral dust and its impact on radiative fluxes as simulated by WRF-Chem, Meteorology and Atmospheric Physics, 127(6), DOI: 10.1007/s00703-015-0390-4, 2015.

Anderson, T. L., Y. Wu, D. A. Chu, B. Schmid, J. Redemann, and O. Dubovik: Testing the MODIS satellite retrieval of aerosol fine-mode fraction, J. Geophys. Res., 110, D18204, doi:10.1029/2005JD005978, 2005.

Angstrom, A. : On the atmospheric transmission of Sun radiation and on dust in the air, Geogr. Ann, 11, 156-166, 1929.

Ault, A. P., C. R. Williams, A. B. White, P. J. Neiman, J. M. Creamean, C. J. Gaston, F. M. Ralph, and K. A. Prather: Detection of Asian dust in California orographic precipitation, J. Geophys. Res., 116, D16205, doi:10.1029/2010JD015351, 2011.

Barnard, J. C., J. D. Fast, G. Paredes-Miranda, W. P. Arnott, and A. Laskin: Technical Note: Evaluation of the WRF-Chem "Aerosol Chemical to Aerosol Optical Properties" Module using data from the MILAGRO campaign, Atmos. Chem. Phys., 10, 7325-7340, doi:10.5194/acp-10-7325-2010, 2010.

891 Barrie, L. A., Y. Yi, W. R. Leaitch, U. Lohmann, P. Kasibhatla, G. J. Roelofs, J. Wilson,
892 F. McGovern, C. Benkovitz, M. A. Melieres, K. Law, J. Prospero, M. Kritz, D.
893 Bergmann, C. Bridgeman, M. Chin, J. Christensen, R. Easter, J. Feichter, C. Land, A.
894 Jeuken, E. Kjellstrom, D. Koch, and P. Rasch: A comparison of large-scale
895 atmospheric sulphate aerosol models (COSAM): overview and highlights, Tellus,
896 53B, 615-645, 2001.
897 Binkowski, F. S., and Shankar, U.: The Regional Particulate Matter Model 1. Model
898 description and preliminary results, J. Geophys. Res., 100(D12), 26191-26209, 1995.
899 Chapman, E. G., Gustafson Jr., W. I., Easter, R. C., Barnard, J. C., Ghan, S. J., Pekour,
900 M. S., and Fast, J. D.: Coupling aerosol-cloud-radiative processes in the WRF-Chem
901 model: Investigating the radiative impact of elevated point sources, Atmos. Chem.
902 Phys., 9, 945–964, doi:10.5194/acp-9-945-2009, 2009.
903 Chen, S., J. Huang, C. Zhao, Y. Qian, L. R. Leung, and B. Yang: Modeling the transport
904 and radiative forcing of Taklimakan dust over the Tibetan Plateau: A case study in the
905 summer of 2006, J. Geophys. Res., 118(2), 797-812, doi:10.1002/jgrd.50122, 2013.
906 Chen, S., C. Zhao, Y. Qian, L. R. Leung, J. Huang, Z. Huang, J. Bi, W. Zhang, J. Shi, L.
907 Yang, D. Li, J. Li: Regional modeling of dust mass balance and radiative forcing over
908 East Asia using WRF-Chem, Aeolian Research, 15, 15-30,
909 doi:10.1016/j.aeolia.2014.02.001, 2014.
910 Chin, M., A. Chu, R. Levy, L. Remer, Y. Kaufman, B. Holben, T. Eck, P. Ginoux, and Q.
911 Gao: Aerosol distribution in the Northern Hemisphere during ACE-Asia: Results
912 from global model, satellite observations, and Sun photometer measurements, J.
913 Geophys. Res., 109, D23S90, doi:10.1029/2004JD004829, 2004.

914 Chin, M., T. Diehl, P. Ginoux, and W. Malm: Intercontinental transport of pollution and
915 dust aerosols: implications for regional air quality, Atmos. Chem. Phys., 7, 5501–
916 5517, 2007.
917 Chow, J. C., L.-W. A. Chen, J. G. Watson, D. H. Lowenthal, K. A. Magliano, K.
918 Turkiewicz, and D. E. Lehrman: PM2.5 chemical composition and spatiotemporal
919 variability during the California Regional PM10/PM2.5 Air Quality Study
920 (CRPAQS), J. Geophys. Res., 111, D10S04, doi:10.1029/2005JD006457, 2006.
921 Creamean, J. M., K. J. Suski, D. Rosenfeld, A. Cazorla, P. J. DeMott, R. C. Sullivan, A.
922 B. White, F. M. Ralph, P. Minnis, J. M. Comstock, J. M. Tomlinson, and K. A.
923 Prather: Dust and Biological Aerosols from the Sahara and Asia Influence
924 Precipitation in the Western U.S., Science, 339, 1572, DOI:
925 10.1126/science.1227279, 2013.
926 Dentener, F., S. Kinne, T. Bond, O. Boucher, J. Cofala, S. Generoso, P. Ginoux, S. Gong,
927 J. J. Hoelzemann, A. Ito, L. Marelli, J. E. Penner, J. P. Putaud, C. Textor, M. Schulz,
928 G. R. van der Werf, and J. Wilson: Emissions of primary aerosol and precursor gases
929 in the years 2000 and 1750 prescribed data-sets for AeroCom: Atmos. Chem. Phys.,
930 6, 4321-4344, 2006.
931 Diner, D. J., J. C. Beckert, T. H. Reilly, C. J. Bruegge, J. E. Conel, R. A. Kahn, J. V.
932 Martonchik, T. P. Ackerman, R. Davies, S. A. W. Gerstl, H. R. Gordon, J. P. Muller,
933 R. B. Myneni, P. J. Sellers, B. Pinty, and M. M. Verstraete: Multi-angle Imaging
934 SpectroRadiometer (MISR) Instrument Description and Experiment Overview, IEEE
935 Trans, Geosci. Remote Sens, 36, 1072-1087, 1998.

936 Dubovik, O. and King, M. D.: A flexible inversion algorithm for retrieval of aerosol
937 optical properties from Sum and sky radiance measurements, J. Geophys. Res.,
938 105(16), 20673-20696, 2000.
939 Dubovik, O., B. N. Holben, T. Lapyonok, A. Sinyuk, M. I. Mishchenko, P. Yang, and I.
940 Slutsker: Non-spherical aerosol retrieval method employing light scattering by
941 spheroids, Geophys. Res. Lett., 29(10), 1415, 10.1029/2001GL014506, 2002.
942 Easter, R. C., Ghan, S. J., Zhang, Y., Saylor, R. D., Chapman, E. G., Laulainen, N. S.,
943 Abdul-Razzak, H., Leung, L. R., Bian, X., and Zaveri, R. A.: MIRAGE: Model
944 Description and Evaluation of Aerosols and Trace Gases, J. Geophys. Res., 109,
945 D20210, doi:10.1029/2004JD004571, 2004.
946 Eck, T. F., B. N. Holben, J. S. Reid, O. Dubovik, A. Smirnov, N. T. O'Neill, I. Slutsker,
947 and S. Kinn: Wavelength dependence of the optical depth of biomass burning urban,
948 and desert dust aerosols, , J. Geophys. Res., 104(24), 31333-31349, 1999.
949 Eguchi, K., I. Uno, K. Yumimoto, T. Takemura, A. Shimizu, N. Sugimoto, and Z. Liu:
950 Trans-pacific dust transport: integrated analysis of NASA/CALIPSO and a global
951 aerosol transport model, Atmos. Chem. Phys., 9, 3137–3145, 2009.
952 Fairlie, T. D., D. J. Jacob, and R. J. Park: The impact of transpacific transport of mineral
953 dust in the United States: Atmospheric Environment, 41, 1251-1266, 2007.
954 Fan, J., L. R. Leung, P. J. DeMott, J. M. Comstock, B. Singh, D. Rosenfeld, J. M.
955 Tomlinson, A. White, K. A. Prather, P. Minnis, J. K. Ayers, and Q. Min: Aerosol
956 impacts on California winter clouds and precipitation during CalWater 2011: local
957 pollution versus long-range transported dust, Atmos. Chem. Phys., 14, 81–101,
958 doi:10.5194/acp-14-81-2014, 2014.

959 Fan, J., D. Rosenfeld, Y. Yang, C. Zhao, L. R. Leung, and Z. Li: Substantial contribution
960 of anthropogenic air pollution to catastrophic floods in Southwest China, Geophys.
961 Res. Lett., 42, 6066-6075, doi:10.1002/2015GL064479, 2015.
962 Fast, J. D., W. I. Gustafson, R. C. Easter, R. A. Zaveri, J. C. Barnard, E. G. Chapman, G.
963 A. Grell, and S. E. Peckham: Evolution of ozone, particulates, and aerosol direct
964 radiative forcing in the vicinity of Houston using a fully coupled meteorology-
965 chemistry- aerosol model, J. Geophys. Res., 111, D21305,
966 doi:10.1029/2005JD006721, 2006.
967 Fast, J., A. C. Aiken, J. Allan, L. Alexander, T. Campos, M. R. Canagaratna, E.
968 Chapman, P. F. DeCarlo, B. de Foy, J. Gaffney, J. de Gouw, J. C. Doran, L. Emmons,
969 A. Hodzic, S. C. Herndon, G. Huey, J. T. Jayne, J. L. Jimenez, L. Kleinman, W.
970 Kuster, N. Marley, L. Russell, C. Ochoa, T. B. Onasch, M. Pekour, C. Song, I. M.
971 Ulbrich, C. Warneke, D. Welsh-Bon, C. Wiedinmyer, D. R. Worsnop, X. Y. Yu, and
972 R. Zaveri: Evaluating simulated primary anthropogenic and biomass burning organic
973 aerosols during MILAGRO: implications for assessing treatments of secondary
974 organic aerosols, Atmos. Chem. Phys., 9, 6191–6215, 2009.
975 Fast, J. D., J. Allan, R. Bahreini, J. Craven, L. Emmons, R. Ferrare, P. L. Hayes, A.
976 Hodzic, J. Holloway, C. Hostetler, J. L. Jimenez, H. Jonsson, S. Liu, Y. Liu, A.
977 Metcalf, A. Middlebrook, J. Nowak, M. Pekour, A. Perring, L. Russell, A. Sedlacek,
978 J. Seinfeld, A. Setyan, J. Shilling, M. Shrivastava, S. Springston, C. Song, R.
979 Subramanian, J. W. Taylor, V. Vinoj, Q. Yang, R. A. Zaveri, and Q. Zhang:
980 Modeling regional aerosol and aerosol precursor variability over California and its
981 sensitivity to emissions and long-range transport during the 2010 CalNex and CARES

campaigns, Atmos. Chem. Phys., 14, 10013–10060, doi:10.5194/acp-14-10013-2014, 2014.

Fischer, E. V., N. C. Hsu, D. A. Jaffe, M.-J. Jeong, and S. L. Gong: A decade of dust: Asian dust and springtime aerosol load in the U.S. Pacific Northwest, Geophys. Res. Lett., 36, L03821, doi:10.1029/2008GL036467, 2009.

Fonseca, R. M., T. Zhang, and K.-T. Yong: Improved simulation of precipitation in the tropics using a modified BMJ scheme in the WRF model, Geosci. Model Dev., 8, 2915–2928, 2015.

Forster, C., O. Cooper, A. Stohl, S. Eckhardt, P. James, E. Dunlea, D. K. Nicks, J. S. Holloway, G. Hubler, D. D. Parrish, T. B. Ryerson, and M. Trainer: Lagrangian transport model forecasts and a transport climatology for the Intercontinental Transport and Chemical Transformation 2002 (ITCT 2K2) measurement campaign, J. Geophys. Res., 109, D07S92, doi:10.1029/2003JD003589, 2004.

Gao, Y., X. Liu, C. Zhao, and M. Zhang: Emission controls versus meteorological conditions in determining aerosol concentrations in Beijing during the 2008 Olympic Games, Atmos. Chem. Phys., 11, 12437–12451, doi:10.5194/acp-11-12437-2011, 2011.

Gao, Y., C. Zhao, X. H. Liu, M. G. Zhang, and L. R. Leung: WRF-Chem simulations of aerosols and anthropogenic aerosol radiative forcing in East Asia, Atmospheric Environment, 92, 250-266, 2014.

Ginoux, P., M. Chin, I. Tegen, J. M. Prospero, B. Holben, O. Dubovik, and S. J. Lin: Sources and distributions of dust aerosols simulated with the GOCART model, J. Geophys. Res., 106(17), 20255-20273, 2001.

1005 Gong, S. L.: A parameterization of sea-salt aerosol source function for sub- and super-
1006 micron particles, Global Biogeochemical Cycle, 17(4), 1097,
1007 doi:10.1029/2003GB002079, 2003.
1008 Grell, G. A., S. E. Peckham, R. Schmitz, S. A. McKeen, G. Frost, W. C. Skamarock, and
1009 B. Eder: Fully coupled ‘‘online’’ chemistry within the WRF model, Atmospheric
1010 Enviroment, 39, 6957-6957, doi:10.1016/j.atmosenv.2005.04.027, 2005.
1011 Gustafson, W. I., E. G. Chapman, S. J. Ghan, R. C. Easter, and J. D. Fast: Impact on
1012 modeled cloud characteristics due to simplified treatment of uniform cloud
1013 condensation nuclei during NEAQS 2004, Geophys. Res. Lett., 34, L19809,
1014 doi:10.1029/2007GL030021, 2007.
1015 Guenther, A; Zimmerman, P; & Wildermuth, M.: Natural volatile organic compound
1016 emission rate estimates for U.S. woodland landscapes. Atmospheric Environment,
1017 28(6), 1197 - 1210. doi: 10.1016/1352-2310(94)90297-6, 1994.
1018 Hadley, O. L., V. Ramanathan, G. R. Carmichael, Y. Tang, C. E. Corrigan, G. C.
1019 Roberts, and G. S. Mauger: Trans-Pacific transport of black carbon and fine aerosols
1020 (D < 2.5 mm) into North America, J. Geophys. Res., 112, D05309,
1021 doi:10.1029/2006JD007632, 2007.
1022 Hadley, O. L., C. E. Corrigan, T. W. Kirchstetter, S. S. Cliff, and V. Ramanathan:
1023 Measured black carbon deposition on the Sierra Nevada snow pack and implication
1024 for snow pack retreat, Atmos. Chem. Phys., 10, 7505-7513, doi:10.5194/acp-10-
1025 7505-2010, 2010.
1026 Hagos, S. M., Z. Feng, C. D. Burleyson, C. Zhao, M. N. Martini, and L. K. Berg: Moist
1027 Process Biases in Simulations of the Madden–Julian Oscillation Episodes Observed

during the AMIE/DYNAMO Field Campaign, J. Climate, DOI: http://dx.doi.org/10.1175/JCLI-D-15-0349.1, 2016.

Hand, J., S. A. Copeland, D. E. Day, A. M. Dillner, H. Indresand, W. C. Malm, C. E. McDade, C. T. Moore, Jr, M. L. Pitchford, B. A. Schichtel, and J. G. Watson: Spatial and seasonal patterns and temporal variability of haze and its constituents in the United States: Report V, June, 2011, available from http://vista.cira.colostate.edu/improve/Publications/ Reports/2011/2011.htm, 2011.

Heald, C. L., D. J. Jacob, R. J. Park, B. Alexander, T. D. Fairlie, R. M. Yantosca, and D. A. Chu: Transpacific transport of Asian anthropogenic aerosols and its impact on surface air quality in the United States, J. Geophys. Res., 111, D14310, doi:10.1029/2005JD006847, 2006.

Hess, M., P. Koepke, and I. Schult: Optical Properties of Aerosols and Clouds: The Software Package OPAC, Bull. Am. Meteorol. Soc., 79(5), 831-844, 1998.

Holben, B. N., T. F. Eck, I. Slutsker, D. Tanre´, J. P. Buis, A. Setzer, E. Vermote, J. A. Reagan, Y. J. Kaufman, T. Nakajima, F. Lavenu, I. Jankowiak, and A. Smirnov: AERONET - A Federated Instrument Network and Data Archive for Aerosol Characterization, Remote Sens. Environ., 66, 1-16, 1998.

Holben, B. N., D. Tanr, A. Smirnov, T. F. Eck, I. Slutsker, N. Abuhassan, W. W. Newcomb, J. S. Schafer, B. Chatenet, F. Lavenu, Y. J.Kaufman, J. V. Castle, A. Setzer, B. Markham, D. Clark, R. Frouin, R. Halthore, A. Karneli, N. T. O'Neill, C. Pietras, R. T. Pinker, K. Voss, and G. Zibordi: An emerginground-basedaerosolclimatology: Aerosol optical depth from AERONET, J. Geophys. Res., 106(11), 12067-12097, 2001.

1051 Hsu, N. C., S. C. Tsay, M. D. King, and J. R. Herman: Deep Blue Retrievals of Asian
1052 Aerosol Properties During ACE-Asia, IEEE Trans, Geosci. Remote Sens., 44(11),
1053 3180-3195, 2006.
1054 Hsu, N. C., M.-J. Jeong, and C. Bettenhausen: Enhanced Deep Blue aerosol retrieval
1055 algorithm: The second generation, J. Geophys. Res. Atmos., 118 (16): 9296–9315,
1056 2013.
1057 Hu, Y., M. Vaughan, Z. Liu, B. Lin, P. Yang, D. Flittner, B. Hunt, R. Kuehn, J. Huang,
1058 D. Wu, S. Rodier, K. Powell, C. Trepte, and D. Winker, The depolarization-
1059 attenuated backscatter relation: CALIPSO lidar measurements vs. theory, *Optics*
1060 *Express*, 15 (9), 5327-5332, 2007.
1061 Hu, Y., D. Winker, M. Vaughan, B. Lin, A. Omar, C. Trepte, D. Flittner, P. Yang, S.
1062 Nasiri, B. Baum, W. Sun, Z. Liu, Z. Wang, S. Young, K. Stamnes, J. Huang, R.
1063 Kuehn, and R. Holz, CALIPSO/CALIOP cloud phase discrimination algorithm,
1064 *Journal of Atmospheric and Oceanic Technology*, 26 (11) (2009), 2293-2309,
1065 doi:10.1175/2009JTECHA1280.1, 2009.
1066 Huang, J., B. Lin, P. Minnis, T. Wang, X. Wang, Y. Hu, Y. Yi, and J. Ayers, Satellite-
1067 based assessment of possible dust aerosols semi-direct effect on cloud water path over
1068 East Asia, *Geophysical Research Letters*, 33 (19), L19802,
1069 doi:10.1029/2006GL026561, 2006.
1070 Huang, J., P. Minnis, B. Chen, Z. Huang, Z. Liu, Q. Zhao, Y. Yi, and J. Ayers, Long-
1071 range transport and vertical structure of Asian dust from CALIPSO and surface
1072 measurements during PACDEX, Journal of Geophysical Research, 113 (D23),
1073 D23212, doi:10.1029/2008JD010620, 2008.

1074 Huang, J., T. Wang, W. Wang, Z. Li, and H. Yan, 2014: Climate effects of dust aerosols
1075 over East Asian arid and semiarid regions, *Journal of Geophysical Research:*
1076 *Atmospheres*, 119, 11398–11416, doi:10.1002/2014JD021796, 2014.
1077 Huang, L., J. H. Jiang, J. L. Tackett, H. Su, and R. Fu: Seasonal and diurnal variations of
1078 aerosol extinction profile and type distribution from CALIPSO 5-year observations, J.
1079 Geophys. Res. Atmos., 118, 4572–4596, doi:10.1002/jgrd.50407, 2013.
1080 Huffman, G. J., R. F. Adler, M. M. Morrissey, D. T. Bolvin, S. Curtis, R. Joyce, B.
1081 McGavock, and J. Susskind: Global Precipitation at One-Degree Daily Resolution
1082 from Multisatellite Observations. J. Hydrometeor, 2, 36–50,doi:
1083 http://dx.doi.org/10.1175/1525-7541(2001)002<0036:GPAODD>2.0.CO;2, 2001.
1084 Iacono, M. J., E. J. Mlawer, S. A. Clough, and J. J. Morcrette: Impact of an
1085 improvedlongwaveradiation model,RRTM, on the energy budget and thermodynamic
1086 properties of the NCAR community climate model, CCM3, J. Geophys. Res.,
1087 105(11), 14873-14890, 2000.
1088 Jaegle, L., P. K. Quinn, T. S. Bates, B. Alexander, and J. T. Lin: Global distribution of
1089 sea salt aerosols: new constraints from in situ and remote sensing observations,
1090 Atmos. Chem. Phys., 11, 3137-3157, doi:10.5194/acp-11-3137-2011, 2011.
1091 Jaffe, D., T. Anderson, D. Covert, R. Kotchenruther, B. Trost, J. Danielson, W. Simpson,
1092 T. Berntsen, S. Karlsdottir, D. Blake, J. Harris, G. Carmichael, and I. Uno: Transport
1093 of Asian Air Pollution to North America, Geophys. Res. Lett., 26(6), 711-714, 1999.
1094 Janssens-Maenhout, G., Crippa, M., Guizzardi, D., Dentener, F., Muntean, M., Pouliot,
1095 G., Keating, T., Zhang, Q., Kurokawa, J., Wankmüller, R., Denier van der Gon, H.,
1096 Kuenen, J. J. P., Klimont, Z., Frost, G., Darras, S., Koffi, B., and Li, M.: HTAP_v2.2:

1097 a mosaic of regional and global emission grid maps for 2008 and 2010 to study
1098 hemispheric transport of air pollution, Atmos. Chem. Phys., 15, 11411-11432,
1099 doi:10.5194/acp-15-11411-2015, 2015.
1100 Jethva, H., O, Torres, and C. Ahn: Global assessment of OMI aerosol single-scattering
1101 albedo using ground-based AERONET inversion, J. Geophys. Res. Atmos., 119,
1102 9020–9040, doi:10.1002/ 2014JD021672, 2014.
1103 Kahn, R. A., D. L. Nelson, M. J. Garay, R. C. Levy, M. A. Bull, D. J. Diner, J. V.
1104 Martonchik, S. R. Paradise, E. G. Hansen, and L. A. Remer: MISR Aerosol Product
1105 Attributes and Statistical Comparisons With MODIS, IEEE Trans, Geosci. Remote
1106 Sens, 47(12), 4095-4114, 2009.
1107 Kaufman, Y. J., D. Tanré, L. A. Remer, E. F. Vermote, A. Chu, and B. N. Holben:
1108 Operational remote sensing of tropospheric aerosol over land from EOS moderate
1109 resolution imaging spectroradiometer, J. Geophys. Res., 102(D14), 17051-17067,
1110 1997.
1111 Kaufman, Y. J., O. Boucher,D. Tanre, M. Chin, L. A. Remer, and T. Takemura: Aerosol
1112 anthropogenic component estimated from satellite data, Geophys. Res. Lett., 32,
1113 L17804, doi:10.1029/2005GL023125, 2005a.
1114 Kaufman, Y. J., I. Koren, L. A. Remer, D. Rosenfeld, and Y. Rudich: The effect of
1115 smoke, dust, and pollution aerosol on shallow cloud development over the Atlantic
1116 Ocean, Proc. Natl. Acad. Sci. USA, 102(32), 11207-11212,
1117 Doi/10.1073/pnas.0505191102, 2005b.

King, M. D., Y. J. Kaufman, D. Tanre, and T. Nakajima: Remote Sensing of Tropospheric Aerosols from Space: Past, Present, and Future, Bull. Am. Meteorol. Soc., 80(11), 2229-2259, 1999.

Kok, J. F.: A scaling theory for the size distribution of emitted dust aerosols suggests climate models underestimate the size of the global dust cycle, Proc. Natl. Acad. Sci. USA, 108(3), 1016-1021, doi/10.1073/pnas.1014798108, 2011.

Koren, I., Y. J. Kaufman, D. Rosenfeld, L. A. Remer, and Y. Rudich: Aerosol invigoration and restructuring of Atlantic convective clouds, Geophys. Res. Lett., 2, L14828, doi:10.1029/2005GL023187, 2005.

Lau, K., V. Ramanathan, G. Wu, Z. Li, S. Tsay, C. Hsu, R. Sikka, B. Holben, D. Lu, G. Tartari, M. Chin, P. Koudelova, H. Chen, Y. Ma, J. Huang, K. Taniguchi, and R. Zhang, The joint aerosol-monsoon experiment: A new challenge for monsoon climate research, *Bulletin of American Meteorological Society*, 89 (3), 369-383, 2008.

Levy, R. C., L. A. Remer, R. G. Keidman, S. Mattoo, C. Ichoku, R. Kahn, and T. F. Eck: Global evaluation of the Collection 5 MODIS dark-target aerosol products over land, Atmos. Chem. Phys., 10, 10399–10420, doi:10.5194/acp-10-10399-2010, 2010.

Levy, R. C., S. Mattoo, L. A. Munchak, L. A. Remer, A. M. Sayer, F. Patadia, and N. Hsu: The Collection 6 MODIS Aerosol Products over Land and Ocean, Atmos. Meas. Tech., 6, 2989-3034 doi:10.5194/amt-6-2989-2013, 2013.

Li, M., Q. Zhang, J. Kurokawa, J. H. Woo, K. B. He, Z. Lu, T. Ohara, Y. Song, D. G. Streets, G. R. Carmichael, Y. F. Cheng, C. P. Hong, H. Huo, X. J. Jiang, S. C. Kang, F. Liu, H. Su, and B. Zheng (2015), MIX: a mosaic Asian anthropogenic emission

1140 inventory for the MICS-Asia and the HTAP projects, Atmos. Chem. Phys. Discuss.,
1141 15(23), 34813-34869, doi:10.5194/acpd-15-34813-2015.
1142 Liang, Q., L. Jaegle, D. A. Jaffe, P. Weiss-Penzias, A. Heckman, and J. A. Snow: Long-
1143 range transport of Asian pollution to the northeast Pacific: Seasonal variations and
1144 transport pathways of carbon monoxide, J. Geophys. Res., 109, D23S07,
1145 doi:10.1029/2003JD004402, 2004.
1146 Liu, Z., M. A. Vaughan, D. M. Winker, C. A. Hostetler, L. R. Poole, D. Hlavka, W. Hart,
1147 abd M. McGill: Use of probability distribution functions for discriminating between
1148 cloud and aerosol in lidar backscatter data, J. Geophys. Res., 109, D15202,
1149 doi:10.1029/2004JD004732, 2004.
1150 Liu, Z., D. Liu, J. Huang, M. Vaughan, I. Uno, N. Sugimoto, C. Kittaka, C. Trepte, Z.
1151 Wang, C. Hostetler, and D. Winker, Airborne dust distributions over the Tibetan
1152 Plateau and surrounding areas derived from the first year of CALIPSO lidar
1153 observations, *Atmospheric Chemistry and Physics*, 8 (16), 5045-5060, 2008.
1154 Lu, Z., Q. Zhang, and D. G. Streets: Sulfur dioxide and primary carbonaceous aerosol
1155 emissions in China and India, 1996–2010, Atmos. Chem. Phys., 11, 9839-9864,
1156 doi:10.5194/acp-11-9839-2011, 2011.
1157 Malm, W. C., J. F. Sisler, D. Huffman, R. A. Eldred, and T. A. Cahill: Spatial and
1158 seasonal trends in particle concentration and optical extinction in the United States,
1159 99(D1), 1347-1370, 1994.
1160 Mao, Y. H., Li, Q. B., Zhang, L., Chen, Y., Randerson, J. T., Chen, D., and Liou, K. N.:
1161 Biomass burning contribution to black carbon in the Western United States Mountain

1162 Ranges, Atmos. Chem. Phys., 11, 11253–11266, doi:10.5194/acp-11- 11253-2011,
1163 2011.
1164 Mao, Y. H., Li, Q. B., Chen, D., Zhang, L., Hao, W.-M., and Liou, K.-N.: Top-down
1165 estimates of biomass burning emissions of black carbon in the Western United States,
1166 Atmos. Chem. Phys., 14, 7195-7211, doi:10.5194/acp-14-7195-2014, 2014.
1167 Martonchik, J. V., David J. D., Kathleen A. C., and M. A. Bull: Regional Aerosol
1168 Retrieval Results From MISR, IEEE Trans, Geosci. Remote Sens, 40(7), 1520-1531,
1169 2002.
1170 McKeen, S. A., G. Wotawa, D. D. Parrish, J. S. Holloway, M. P. Buhr, G. Hubler, F. C.
1171 Fehsenfeld, and J. F. Meagher: Ozone production from Canadian wildfires during
1172 June and July of 1995, J. Geophys. Res., 107(D14), 4192, 10.1029/2001JD000697,
1173 2002.
1174 Mlawer, E. J., S. J. Taubman, P. D. Brown, M. J. Iacono, and S. A. Clough: Radiative
1175 transfer for inhomogeneous atmospheres: RRTM, a validated correlated-k model for
1176 the longwave, J. Geophys. Res., 102(D14), 16663-16682, 1997.
1177 Painter, T. H., J. S. Deems, J. Belnap, A. F. Hamlet, C. C. Landry, and B. Udall:
1178 Response of Colorado River runoff to dust radiative forcing in snow, Proc. Natl.
1179 Acad. Sci. USA, 107(40), 17125-17130, doi/10.1073/pnas.0913139107, 2010.
1180 Penner, J. E., S. Y. Zhang, M. Chin, C. C. Chuang, J. Fechter, Y. Feng, I. V.
1181 Geogdzhayev, P. Ginoux, M. Herzog, A. Higurashi, D. Koch, C. Land, U. Lohmann,
1182 M. Mischecko, T. Nakajima, G. Pitari, B. Soden, I. Tegen, and L. Stowe: A
1183 Comparison of Model- and Satellite-Derived Aerosol Optical Depth and Reflectivity,
1184 J. Atmos. Sci., 59, 441-460, 2002.

1185 Qian, Y., W. I. Gustafson, L. R. Leung, and S. J. Ghan: Effects of soot-induced snow
1186 albedo change on snowpack and hydrological cycle in western United States based on
1187 Weather Research and Forecasting chemistry and regional climate simulations, J.
1188 Geophys. Res., 114, D03108, doi:10.1029/2008JD011039, 2009.
1189 Qian, Y., W. I. Gustafson Jr. and J. D. Fast: An investigation of the sub-grid variability of
1190 trace gases and aerosols for global climate modeling, Atmos. Chem. Phys., 10, 6917-
1191 6946, doi:10.5194/acp-10-6917-2010, 2010.
1192 Qian, Y., H. Yan, Z. Hou, C. Johannesson, S. Klein, D. Lucas, R. Neale, P. Rasch, L.
1193 Swiler, J. Tannahill, H. Wang, M. Wang, and C. Zhao: Parametric sensitivity analysis
1194 of precipitation at global and local scales in the Community Atmosphere Model
1195 CAM5, J. Adv. Model. Earth Syst., 7, 382-411, doi:10.1002/2014MS000354, 2015.
1196 Remer, L. A., Y. J. Kaufman, D. Tanre, S. Mattoo, D. A. Chu, J. V. Martins, R. R. Li, C.
1197 Ichoku, R. C. Levy, R. G. Kleidman, T. F. Eck, E. Vermote, and B. N. Holben: The
1198 MODIS aerosol algorithm, products and validation, J. Atmos. Sci., 62, 947-973,
1199 2005.
1200 Remer, L. A. and Kaufman, Y. J.: Aerosol direct radiative effect at the top of the
1201 atmosphere over cloud free ocean derived from four years of MODIS data, Atmos.
1202 Chem. Phys., 6, 237–253, 2006.
1203 Rienecker, M. M., M. J. Suarez, R. Gelaro, R. Todling, J. Bacmeister, E. Liu, M. G.
1204 Bosilovich, S. D. Schubert, L. Takacs, G.-K. Kim, S. Bloom, J. Chen, D. Collins, A.
1205 Conaty, A. da Silva, W. Gu, J. Joiner, R. D. Koster, R. Lucchesi, A. Molod, T.
1206 Owens, S. Pawson, P. Pegion, C. R. Redder, R. Reichle, F. R. Robertson, A. G.
1207 Ruddick, M. Sienkiewicz, and J. Woollen: MERRA: NASA's Modern-Era

1208 Retrospective Analysis for Research and Applications. J. Climate, 24, 3624–3648.
1209 doi: http://dx.doi.org/10.1175/JCLI-D-11-00015.1, 2011.
1210 Sassen, K.: Indirect climate forcing over the western US from Asian Dust strom,
1211 Geophys. Res. Lett., 29(10), 1465, 10.1029/2011GL014051, 2002.
1212 Schulz, M., C. Textor, S. Kinne, Y. Balkanski, S. Bauer, T. Berntsen, T. Berglen, O.
1213 Boucher, F. Dentener, S. Guibert, I. S. A. Isaksen, T. Iversen, D. Koch, A. Kirkevag,
1214 X. Liu, V. Montanaro, G. Myhre, J. E. Penner, G. Pitari, S. Reddy, Ø. Seland, P.
1215 Stier, and T. Takemura: Radiative forcing by aerosols as derived from the AeroCom
1216 present-day and pre-industrial simulations, Atmos. Chem. Phys., 6, 5225–5246, 2006.
1217 Schuster, G. L., O. Dubovik, and B. N. Holben: Angstrom exponent and bimodal aerosol
1218 size distributions, J. Geophys. Res., 111, D07207, doi:10.1029/2005JD006328, 2006.
1219 Shrivastava, M., J. Fast, R. Easter, W. I. Gustafson, R. A. Zaveri, J. L. Jimenez, P. Saide,
1220 and A. Hodzic: Modeling organic aerosols in a megacity: comparison of simple and
1221 complex representations of the volatility basis set approach, 11, 6639–6662,
1222 doi:10.5194/acp-11-6639-2011, 2011.
1223 Skamarock, W. C. and Klemp, J. B.: A time-split nonhydrostatic atmospheric model for
1224 weather research and forecasting applications, J. Com. Phy., 227, 3456-3485,
1225 doi:10.1016/j.jcp.2007.01.037, 2008.
1226 Smirnov, A., B. N. Holben, T. F. Eck, O. Dubovik, and I. Slutsker: Effect of wind speed
1227 on columnar aerosol optical properties at Midway Island, J. Geophys. Res., 108,
1228 4802, doi:10.1029/2003JD003879, D24, 2003.

1229 Stauffer, D. R. and Seaman, N. L.: Use of Four-Dimensional Data Assimilation in a
1230 Limited_Area Mesoscale Model. Part I: Experiments with Synoptic-Scale Data, Mon.
1231 Wea. Rev., 118, 1250-1277, 1990.
1232 Takemura T, Nakajima T, Dubovik O, Holben BN, Kinne S. Single-scattering albedo and
1233 radiative forcing of various aerosol species with a global three-dimensional model. J
1234 Climate,15:333–52,2002.
1235 Tao, Z., H. Yu, and M. Chin, Impact of transpacific aerosol on air quality over the United
1236 States: A perspective from aerosol-cloud-radiation interactions, Atmos. Environ.,
1237 125, 48-60, 2016.
1238 Textor, C., M. Schulz, S. Guibert, S. Kinne, Y. Balkanski, S. Bauer, T. Berntsen, T.
1239 Berglen, O. Boucher, M. Chin, F. Dentener, T. Diehl, R. Easter, H. Feichter, D.
1240 Fillmore, S. Ghan, P. Ginoux, S. Gong, A. Grini, J. Hendricks, L. Horowitz, P.
1241 Huang, I. Isaksen, T. Iversen, S. Kloster, D. Koch, A. Kirkevag, J. E. Kristjansson,
1242 M. Krol, A. Lauer, J. F. Lamarque, X. Liu, V. Montanaro, G. Myhre, J. Penner, G.
1243 Pitari, S. Reddy, Ø. Seland, P. Stier, T. Takemura, and X. Tie: Analysis and
1244 quantification of the diversities of aerosol life cycles within AeroCom, Atmos. Chem.
1245 Phys., 6, 1777–1813, 2006.
1246 Torres, O., C. Ahn, and Z. Chen: Improvements to the OMI near-UV aerosol algorithm
1247 using A-train CALIOP and AIRS observations, Atmos. Meas. Tech., 6, 3257–3270,
1248 doi:10.5194/amt-6-3257-2013, 2013.
1249 Uno, I., K. Eguchi, K. Yumimoto, T. Takemura, A. Shimizu, M. Uematsu, Z. Liu, Z.
1250 Wang, Y. Hara, and N. Sugimoto: Asian dust transported one full circuit around the
1251 globe, Nature Geoscience, 557-560, doi:10.1038/ngeo583, 2009.

1252 Uno, I., Eguchi, K., Yumimoto, K., Liu, Z., Hara, Y., Sugimoto, N., Shimizu, A., and
1253 Takemura, T.: Large Asian dust layers continuously reached North America in April
1254 2010, Atmos. Chem. Phys., 11, 7333-7341, doi:10.5194/acp-11-7333-2011, 2011.
1255 VanCuren, R. A.: Asian aerosols in North America: Extracting the chemical composition
1256 and mass concentration of the Asian continental aerosol plume from long-term
1257 aerosol records in the western United States, J. Geophys. Res., 108, NO. D20, 4623,
1258 doi:10.1029/2003JD003459, 2003.
1259 van der Werf, G. R., J. T. Randerson, L. Giglio, G. J. Collatz, M. Mu, P. S. Kasibhatla, D.
1260 C. Morton, R. S. DeFries, Y. Jin, and T. T. van Leeuwen: Global fire emissions and
1261 the contribution of deforestation, savanna, forest, agricultural, and peat fires (1997–
1262 2009), Atmos. Chem. Phys., 10, 11707–11735, doi:10.5194/acp-10-11707-2010,
1263 2010.
1264 Veihelmann, B., P. F. Levelt, P. Stammes, and J. P. Veefkind: Simulation study of the
1265 aerosol information content in OMI spectral reflectance measurements, Atmos.
1266 Chem. Phys., 7, 3115–3127, 2007.
1267 Wiedinmyer, C., S. K. Akagi, R. J. Yokelson, L. K. Emmons, J. A. Al-Saadi, J. J.
1268 Orlando, and A. J. Soja. "The Fire Inventory from Ncar (Finn): A High Resolution
1269 Global Model to Estimate the Emissions from Open Burning." Geoscientific Model
1270 Development 4, no. 3 (2011): 625-41, 2011.
1271 Winker, D. M., W. H. Hunt, and M. J. McGill: Initial performance assessment of
1272 CALIOP, J. Geophys. Res., 34, L19803, doi:10.1029/2007GL030135, 2007.
1273 Winker, D. M., M. A. Vaughan, A. Omar, Y. Hu, K. A. Powell, Z. Liu, W. H. Hunt, and
1274 S. A. Young: Overview of the CALIPSO Mission and CALIOP Data Processing

1275 Algorithms, J. Atmos. Oceanic Technol., 26, 2310–2323, doi:
1276 http://dx.doi.org/10.1175/2009JTECHA1281.1, 2009.
1277 Yu, H. B., R. E. Dickinson, M. Chin, Y. J. Kaufman, B. N. Holben, I. V. Geogdzhayev,
1278 and M. I. Mishchenko: Annual cycle of global distributions of aerosol optical depth
1279 from integration of MODIS retrievals and GOCART model simulations, J. Geophys.
1280 Res.,108, NO. D3, 4128, doi:10.1029/2002JD002717, 2003.
1281 Yu, H. B., R. E. Dickinson, M. Chin, Y. J. Kaufman, M. Zhou, L. Zhou, Y. Tian, O.
1282 Dubovik, and B. N. Holben: Direct radiative effect of aerosols as determined from a
1283 combination of MODIS retrievals and GOCART simulations, J. Geophys. Res.,109,
1284 D03206, doi:10.1029/2003JD003914, 2004.
1285 Yu, H. B., R. Fu, R. E. Dickinson, Y. Zhang, M. Chen, and H. Wang, Interannual
1286 variability of smoke and warm cloud relationships in the Amazon as inferred from
1287 MODIS retrievals, Remote Sens. Environ., 111, 435-449,
1288 doi:10.1016/j.rse.2007.04.003, 2007.
1289 Yu, H. B., L. A. Remer, M. Chin, H. S. Bian, R. G. Kleidman, and T. Diehl: A satellite-
1290 based assessment of transpacific transport of pollution aerosol, J. Geophys. Res., 113,
1291 D14S12, doi:10.1029/2007JD009349, 2008.
1292 Yu, H., M. Chin, L. A. Remer, R. G. Kleidman, N. Bellouin, H. Bian, and T. Diehl:
1293 Variability of marine aerosol fine-mode fraction and estimates of anthropogenic
1294 aerosol component over cloud-free oceans from MODIS, J. Geophys. Res., 114,
1295 D10206, doi:10.1029/2008JD010648, 2009.
1296 Yu, H. B., M. Chin, D. M. Winker, A. H. Omar, Z. Y. Liu, C. Kittaka, and T. Diehl:
1297 Global view of aerosol vertical distributions from CALIPSO lidar measurements and

1298 GOCART simulations: Regional and seasonal variations, J. Geophys. Res.,115,
1299 D00H30, doi:10.1029/2009JD013364, 2010.
1300 Yu, H., L. A. Remer, M. Chin, H. Bian, Q. Tan, T. Yuan, and Y. Zhang: Aerosols from
1301 Overseas Rival Domestic Emissions over North America, Science, 337, 566-569,
1302 2012.
1303 Yu, H., M. Chin, H. Bian, T. L. Yuan, J. M. Prospero, A. H. Omar, L. A. Remer, D. M.
1304 Winker, Y. Yang, Y. Zhang, and Z. Zhang: Quantification of trans-Atlantic dust
1305 transport from seven-year (2007-2013) record of CALIPSO lidar measurements,
1306 Remote Sens. Environ., 159, 232-249, http://dx.doi.org/10.1016/j.rse.2014.12.010,
1307 2015.
1308 Zaveri, R. A. and Peters, L. K.: A new lumped structure photochemical mechanism for
1309 large-scale applications, J. Geophys. Res., 104(D23), 30387-30415, 1999.
1310 Zaveri, R. A., R. C. Easter, J. D. Fast, and L. K. Peters: Model for Simulating Aerosol
1311 Interactions and Chemistry (MOSAIC), J. Geophys. Res., 113, D13204,
1312 doi:10.1029/2007JD008782, 2008.
1313 Zhang, J. and Reid, J. S.: MODIS aerosol product analysis for data assimilation:
1314 Assessment of over-ocean level 2 aerosol optical thickness retrievals, J. Geophys.
1315 Res., 111, D22207, doi:10.1029/2005JD006898, 2006.
1316 Zhang, Q., D. G. Streets, G. R. Carmichael, K. B. He, H. Huo, A. Kannari, Z. Klimont, I.
1317 S. Park, S. Reddy, J. S. Fu, D. Chen, L. Duan, Y. Lei, L. T. Wang, and Z. L. Yao:
1318 Asian emissions in 2006 for the NASA INTEX-B mission, Atmos. Chem. Phys., 9,
1319 5131–5153, 2009.

1320 Zhao, C., X. Liu, L. R. Leung, B. Johnson, S. A. McFarlane, W. I. Gustafson, J. D. Fast,
1321 and R. Easter: The spatial distribution of mineral dust and its shortwave radiative
1322 forcing over North Africa: modeling sensitivities to dust emissions and aerosol size
1323 treatments, Atmos. Chem. Phys., 10, 8821–8838, doi:10.5194/acp-10-8821-2010,
1324 2010a.
1325 Zhao, C., Y. Wang, Q. Yang, R. Fu, and Y. Choi: Impact of East Asia summer monsoon
1326 on the air quality over China: view from space, J. Geophys. Res., 115, D09301,
1327 doi:10.1029/2009JD012745, 2010.
1328 Zhao, C., X. Liu, L. R. Leung, and S. Hagos: Radiative impact of mineral dust on
1329 monsoon precipitation variability over West Africa, Atmos. Chem. Phys., 11, 1879-
1330 1893, doi:10.5194/acp-11-1879-2011, 2011.
1331 Zhao, C., X. Liu, and L. R. Leung: Impact of the Desert dust on the summer monsoon
1332 system over Southwestern North America, Atmos. Chem. Phys., 12, 3717–3731, d
1333 oi:10.5194/acp-12-3717-2012, 2012.
1334 Zhao, C., L. R. Leung, R. Easter, J. Hand, and J. Avise: Characterization of speciated
1335 aerosol direct radiative forcing over California, J. Geophys. Res., 118, 2372–2388,
1336 doi:10.1029/2012JD018364, 2013a.
1337 Zhao, C., S. Chen, L. R. Leung, Y. Qian, J. F. Kok, R. A. Zaveri, and J. Huang:
1338 Uncertainty in modeling dust mass balance and radiative forcing from size
1339 parameterization, Atmos. Chem. Phys., 13, 10733–10753, doi:10.5194/acp-13-10733-
1340 2013, 2013b.
1341 Zhao, C., Z. Hu, Y. Qian, L. R. Leung, J. Huang, M. Huang, J. Jin, M. G. Flanner, R.
1342 Zhang, H. Wang, H. Yan, Z. Lu, and D. G. Streets: Simulating black carbon and dust

and their radiative forcing in seasonal snow: a case study over North China with field campaign measurements, Atmos. Chem. Phys., 14, 11475–11491, doi:10.5194/acp-14-11475-2014, 2014.

Zhao, C., M. Huang, J. Fast, L. Berg, Y. Qian, A. Guenther, D. Gu, M. Shrivastava, Y. Liu, S. Walters, G. Pfister, J. Jin: Sensitivity of biogenic volatile organic compounds (BVOCs) to land surface processes and vegetation distributions in California, Geosci. Model Dev. Discuss., doi:10.5194/gmd-2015-266, in review, 2016.

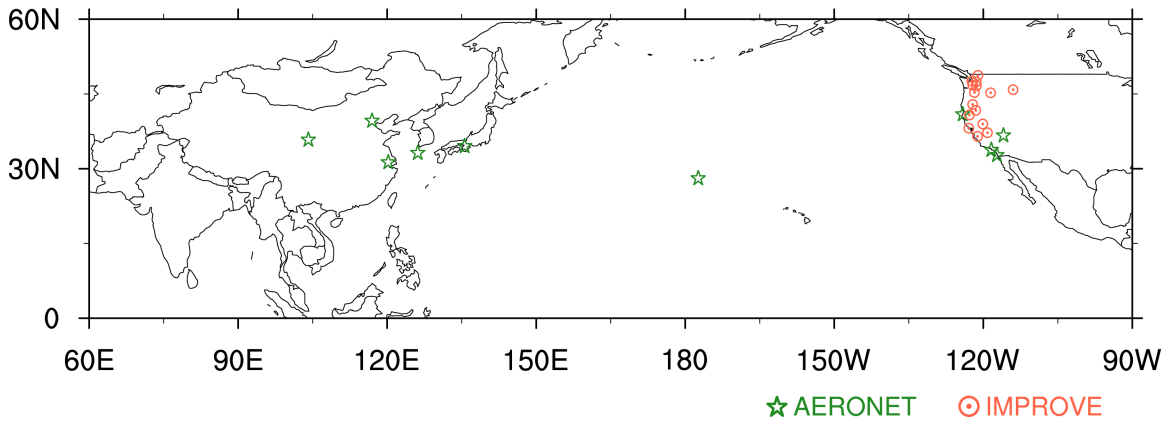


**Figure 1** Observation sites for the AERONET (green stars) and IMPROVE (red dot circles) networks used in this study.

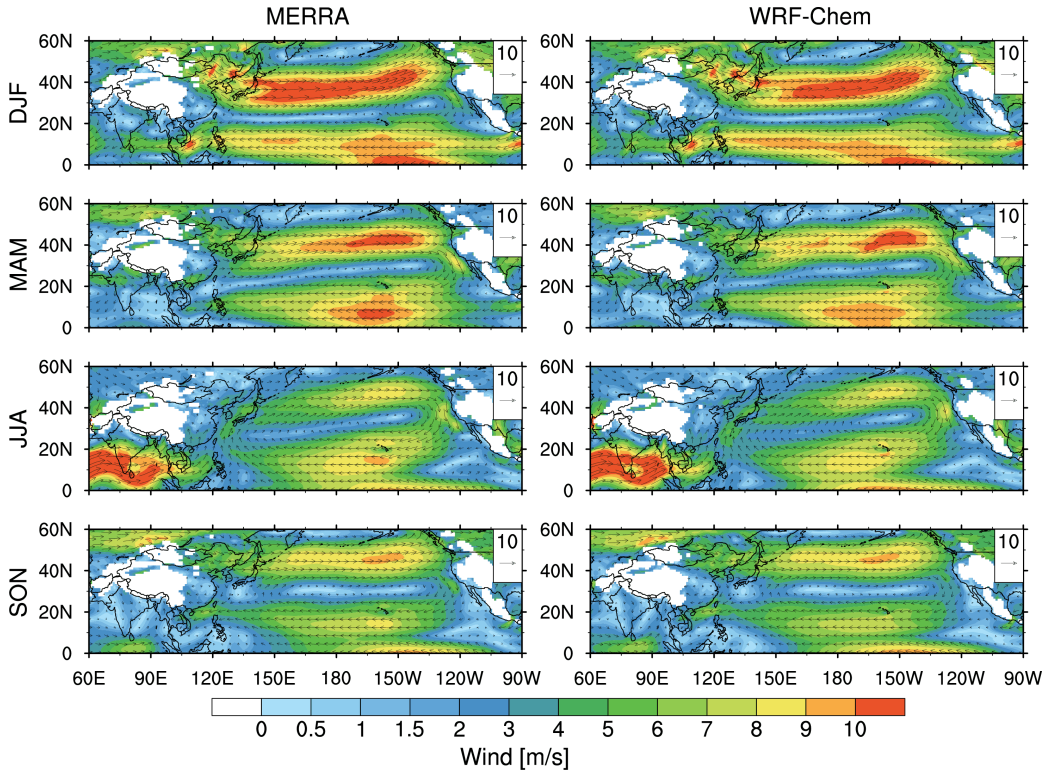


**Figure 2** Spatial distributions of seasonal averaged wind fields at 850 hPa from the MERRA reanalysis and the WRF-Chem simulation for the period 2010-2014.

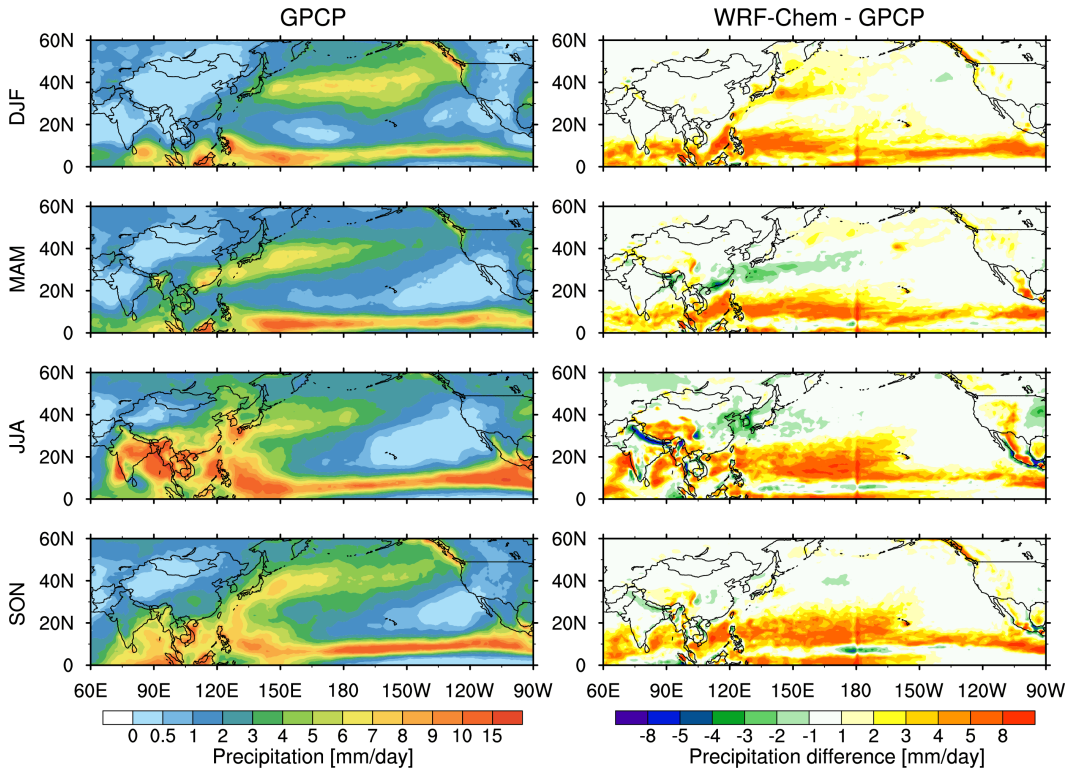


**Figure 3** Spatial distributions of seasonal averaged precipitation from the GPCP observation and the difference between observation and simulation for the period 2010-2014.

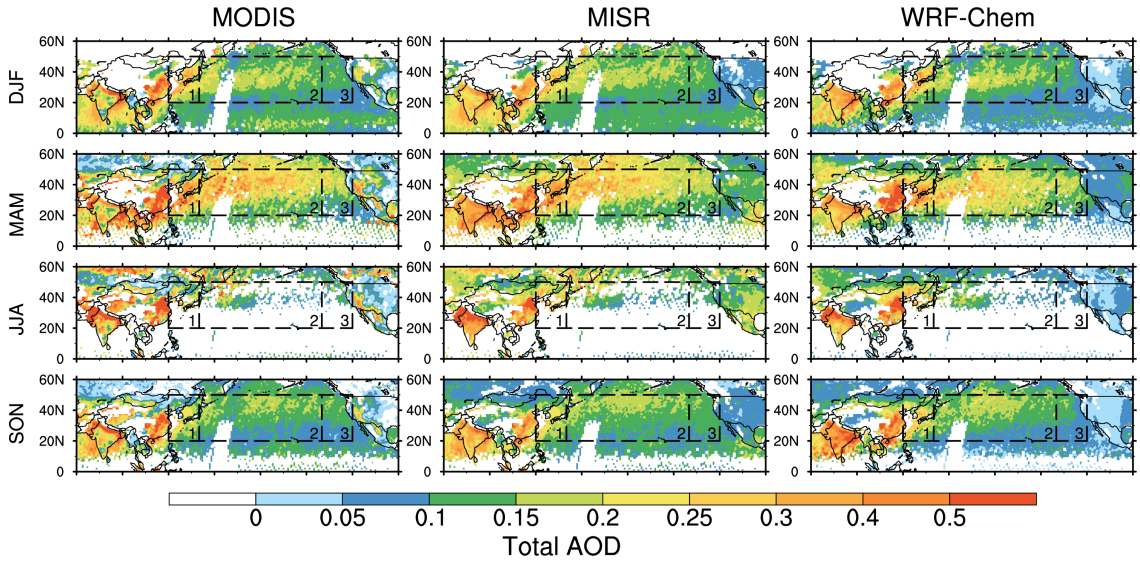


**Figure 4** Spatial distributions of seasonal mean 550 nm AOD from the retrievals of MODIS and MISR onboard Terra and the WRF-Chem simulation for the period 2010-2014. The daily results from MISR, MODIS, and WRF-Chem are only sampled for averaging when all of them have valid values at the same location and time. Three sub-regions are denoted by the black boxes: Region 1 (20°N-50°N and 120°E-140°E), Region 2 (20°N-50°N and 140°E-140°W), and Region 3 (20°N-50°N and 140°W-120°W).

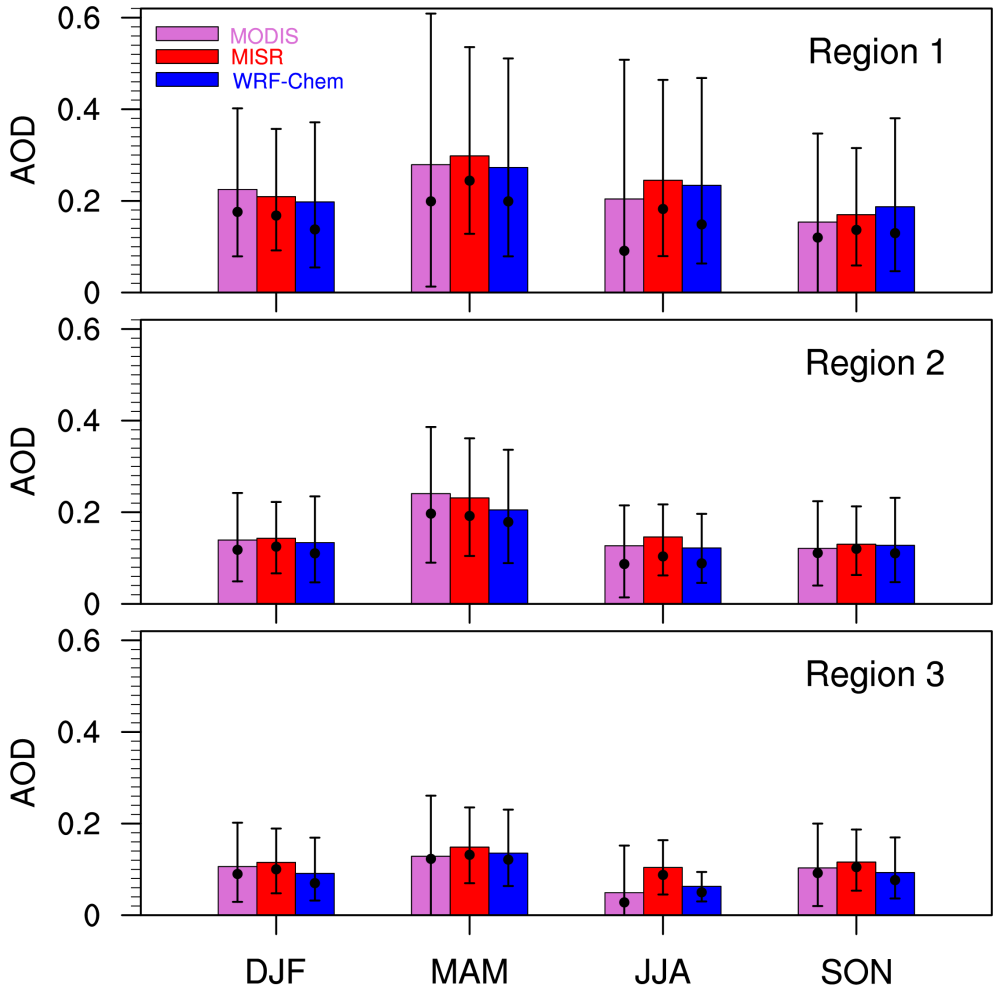


**Figure 5** Seasonal mean 550 nm AOD from the MISR and MODIS retrievals, and the corresponding WRF-Chem simulation averaged for the period 2010-2014 over the three sub-regions shown in Fig. 4. The values of bars represent the mean. The vertical lines represent 10$^{th}$ and 90$^{th}$ percentile values, and the black dots represent the median values.

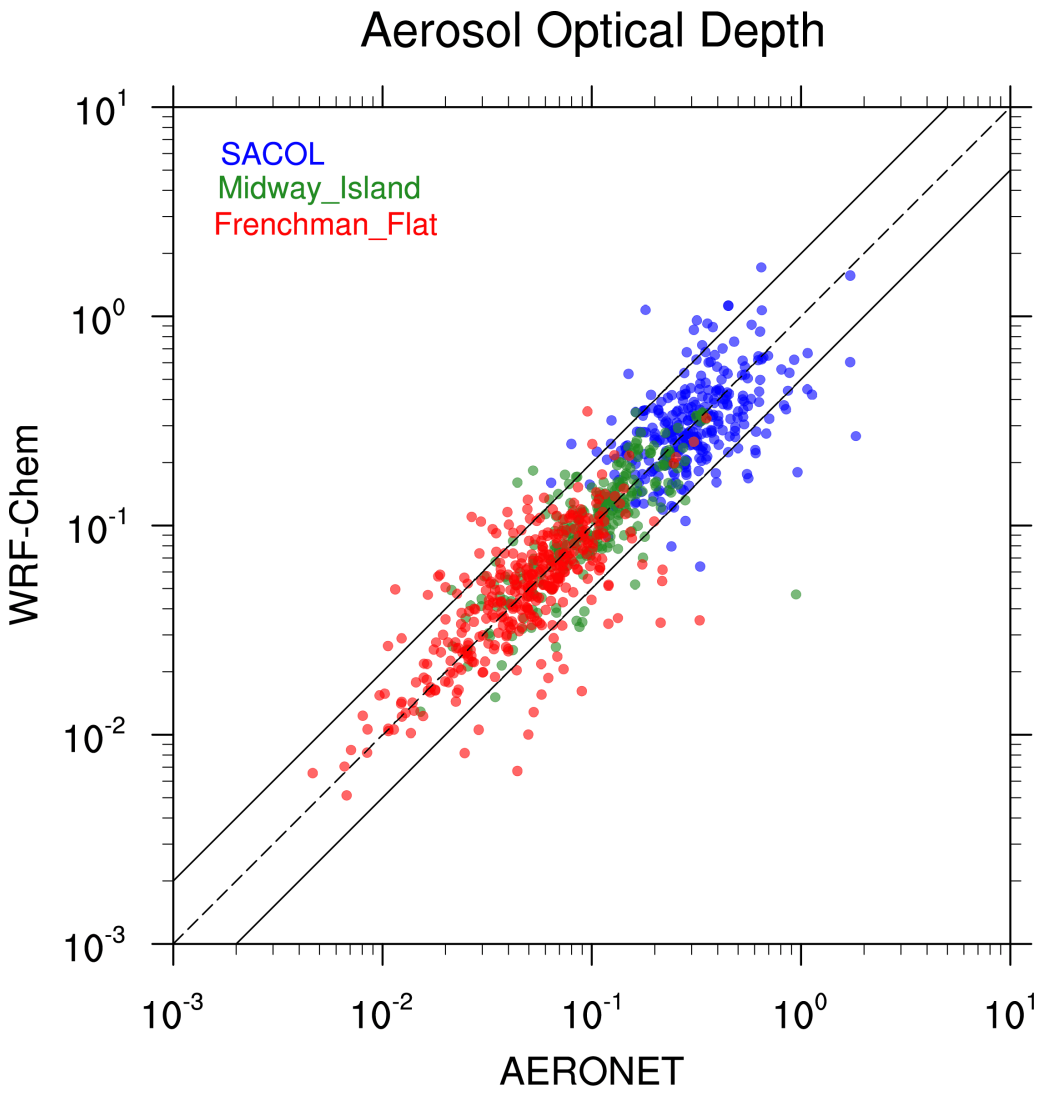


**Figure 6** The AERONET observations of daily AOD at 550 nm at the three sites (SACOL, Midway Island, and Frenchman Flat) versus the corresponding WRF-Chem simulation for the period 2010-2014.

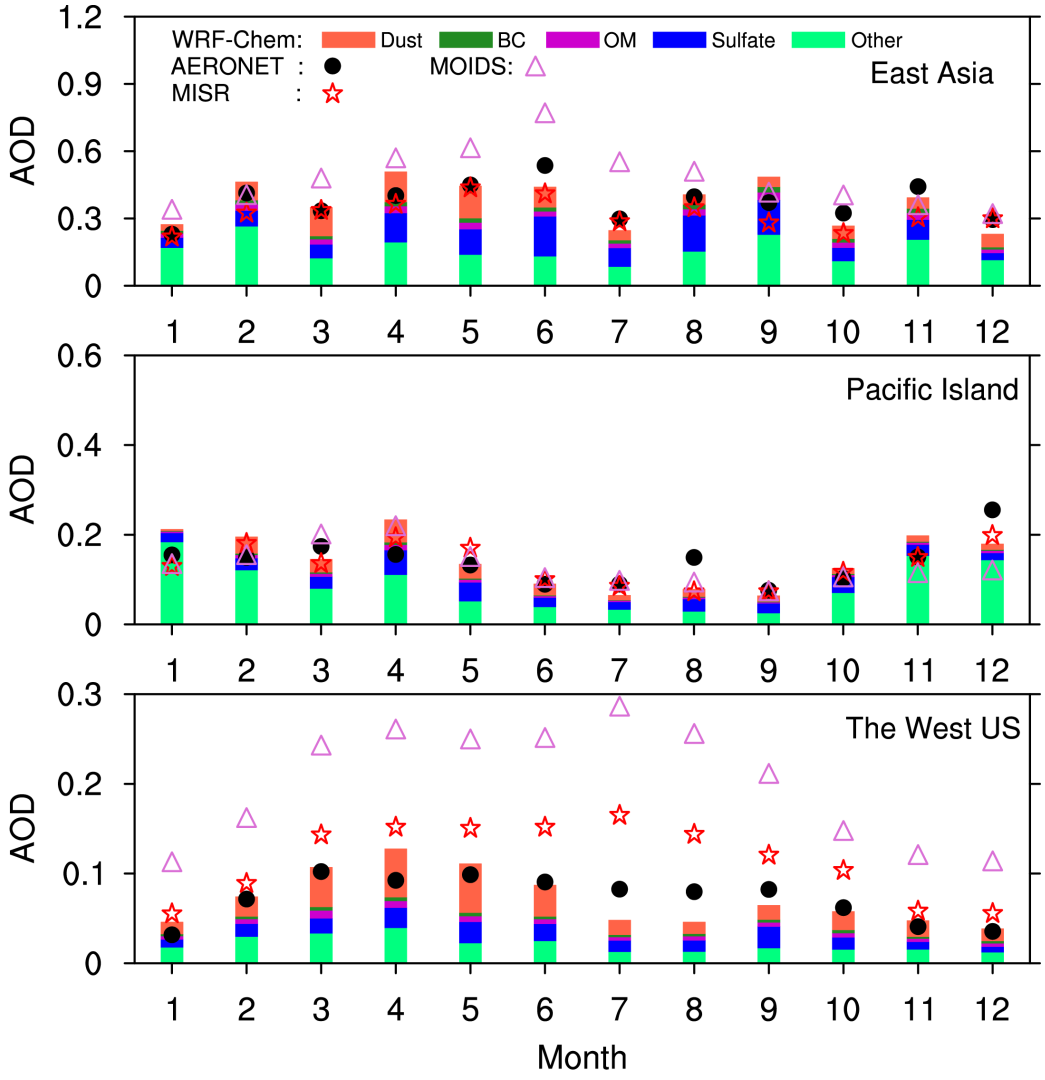


**Figure 7** Monthly mean 550 nm AOD from AERONET (black dots), MODIS (purple triangles), MISR (red five-pointed stars) and the corresponding WRF-Chem simulation (histogram) averaged for the period 2010-2014 at the East Asian, the Pacific island, and the West U.S. sites as shown in Fig. 1.

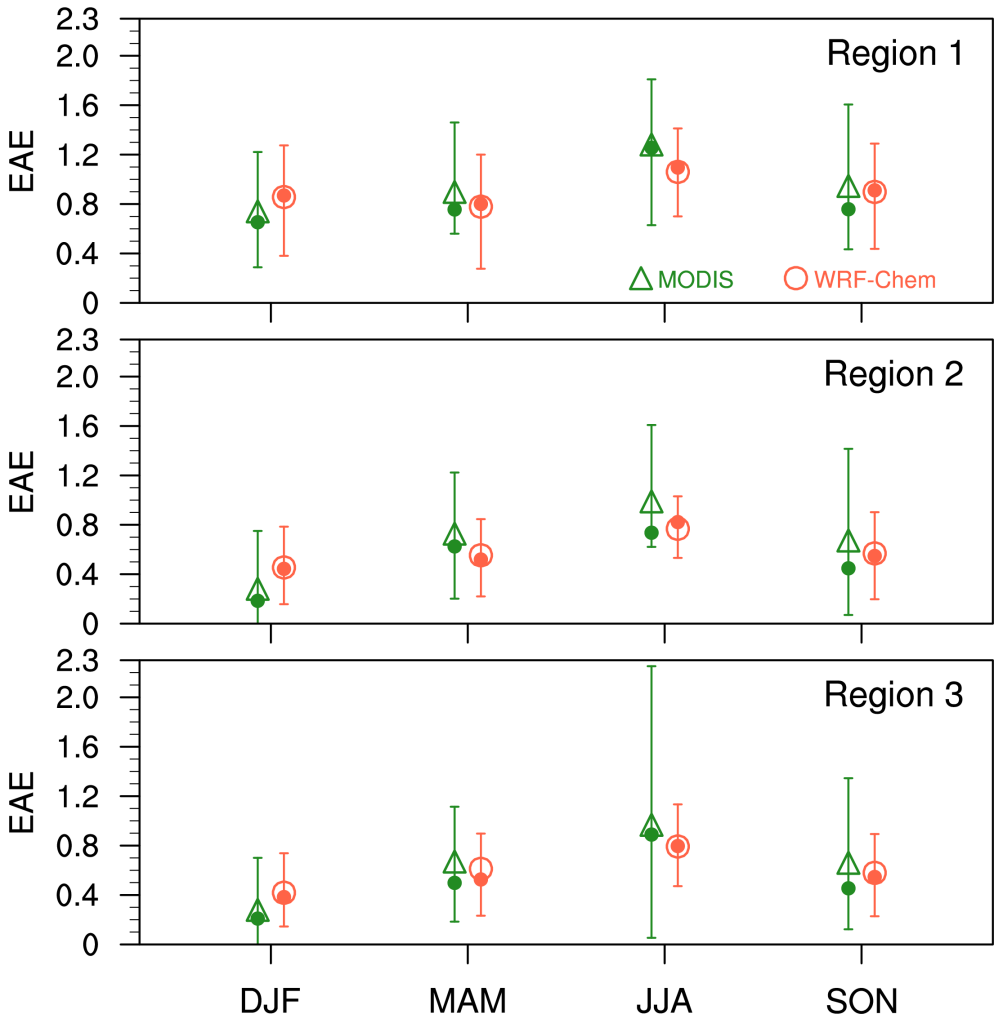


**Figure 8** Seasonal mean EAE from the MODIS retrievals and the corresponding WRF-Chem simulation averaged for the period 2010-2014 over the three sub-regions shown in Fig. 4. The vertical bars represent 10$^{th}$ and 90$^{th}$ percentile values, the filled dots represent the median values, and the triangles and circles represent the mean values.

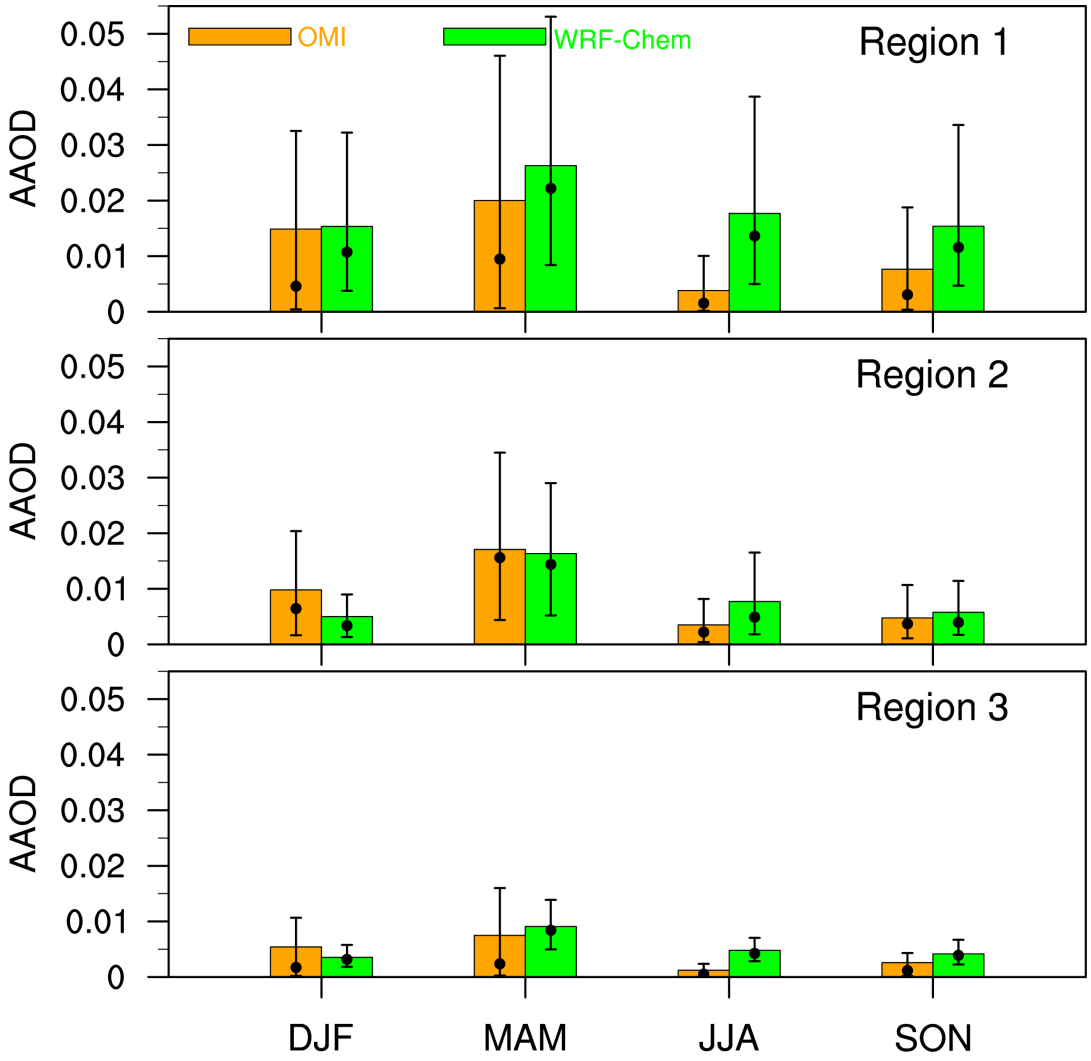


**Figure 9** Seasonal mean AAOD at 500 nm from the OMI retrievals and the corresponding WRF-Chem simulation averaged for the period 2010-2014 over the three sub-regions shown in Fig. 4. The values of bars represent the mean. The vertical lines represent $10^{th}$ and $90^{th}$ percentile values, and the black dots represent the median values.

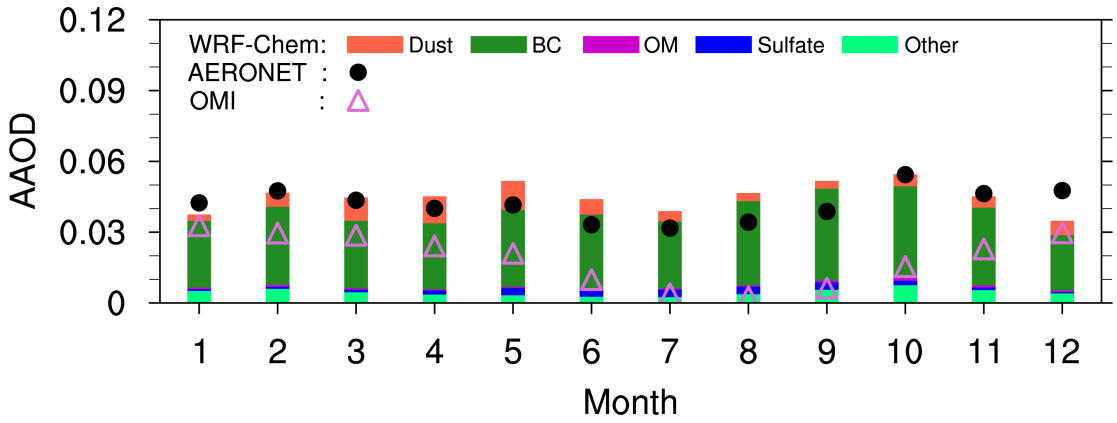


**Figure 10** Monthly AAOD from the retrievals of AERONET and OMI and the corresponding WRF-Chem simulation averaged for the period 2010-2014 over the East Asia sites as shown in Fig. 1.

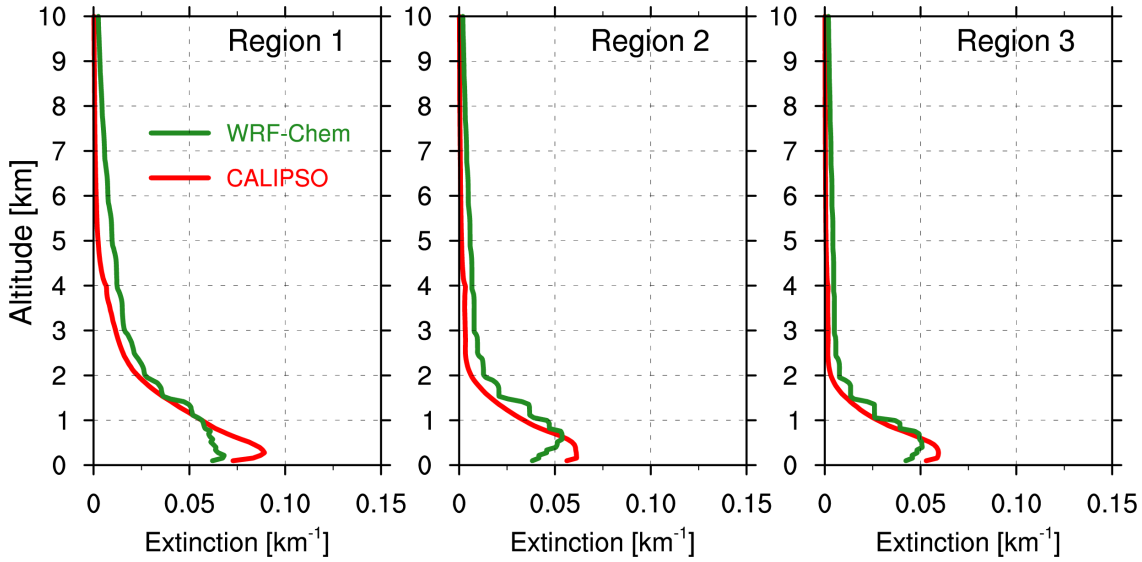


**Figure 11** Vertical distributions of annual mean extinction from the CALIPSO retrieval and the corresponding WRF-Chem simulation averaged for the period 2010-2014 over the three sub-regions shown in Fig. 4.

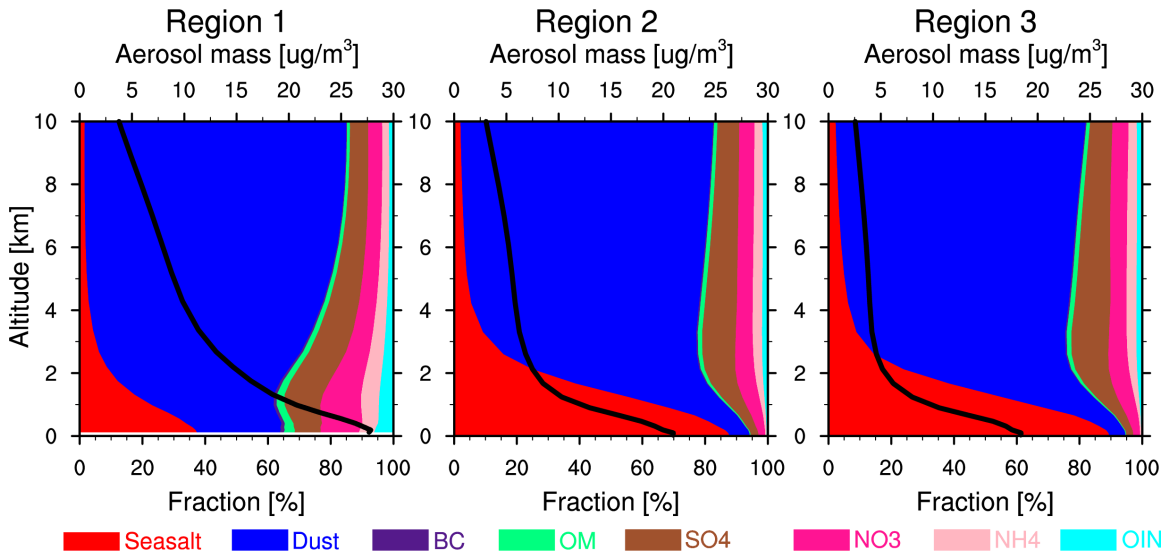


**Figure 12** Vertical distributions of annual mean aerosol mass (black solid line; upper X-axis) and its composition fractions (colored shade-contour; lower X-axis) from the WRF-Chem simulation averaged for the period 2010-2014 over three sub-regions as shown in Fig. 4.

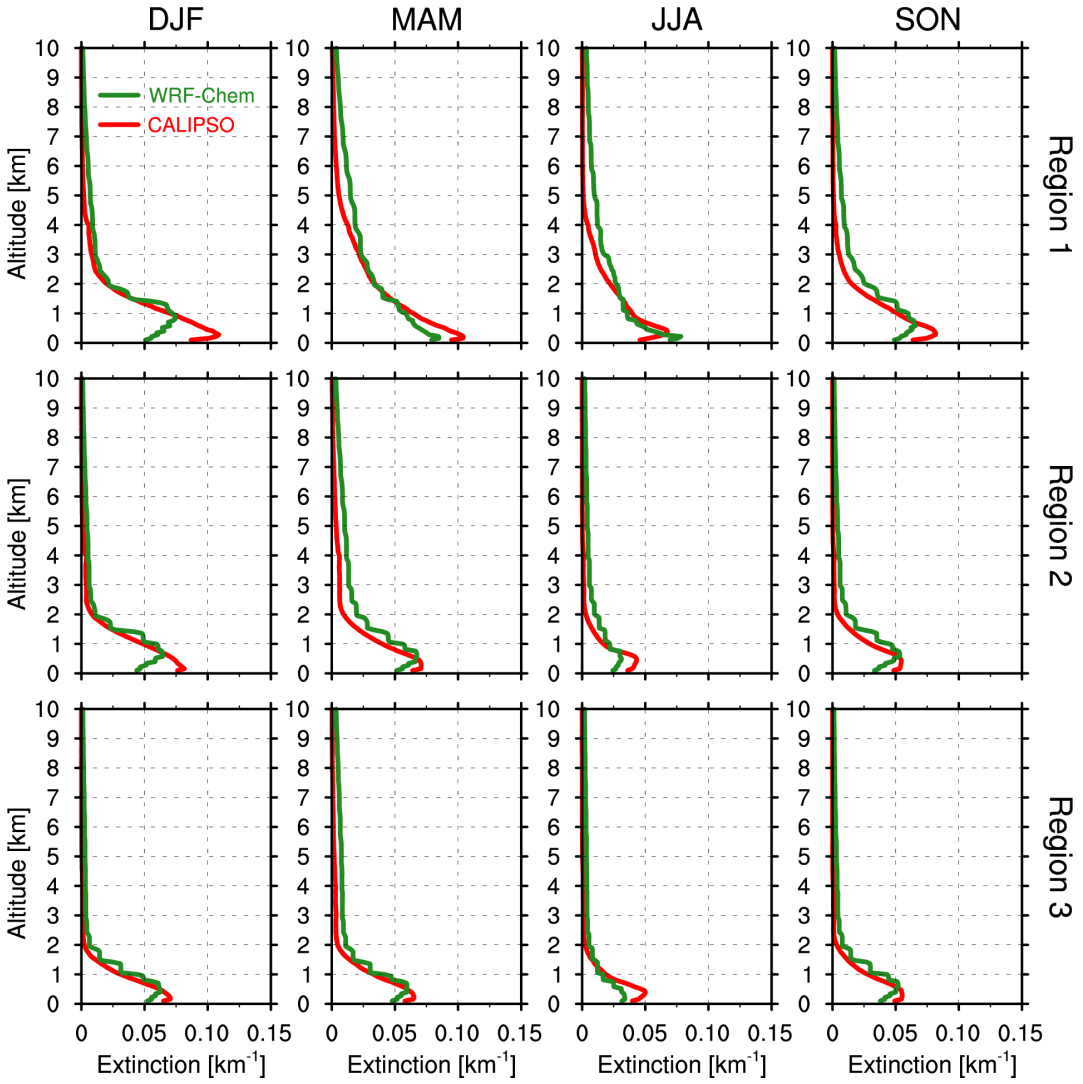


**Figure 13** Vertical distributions of seasonal mean aerosol extinction from the CALIPSO retrieval and the corresponding WRF-Chem simulation averaged for the period 2010-2014 over three sub-regions as shown in Fig. 4.

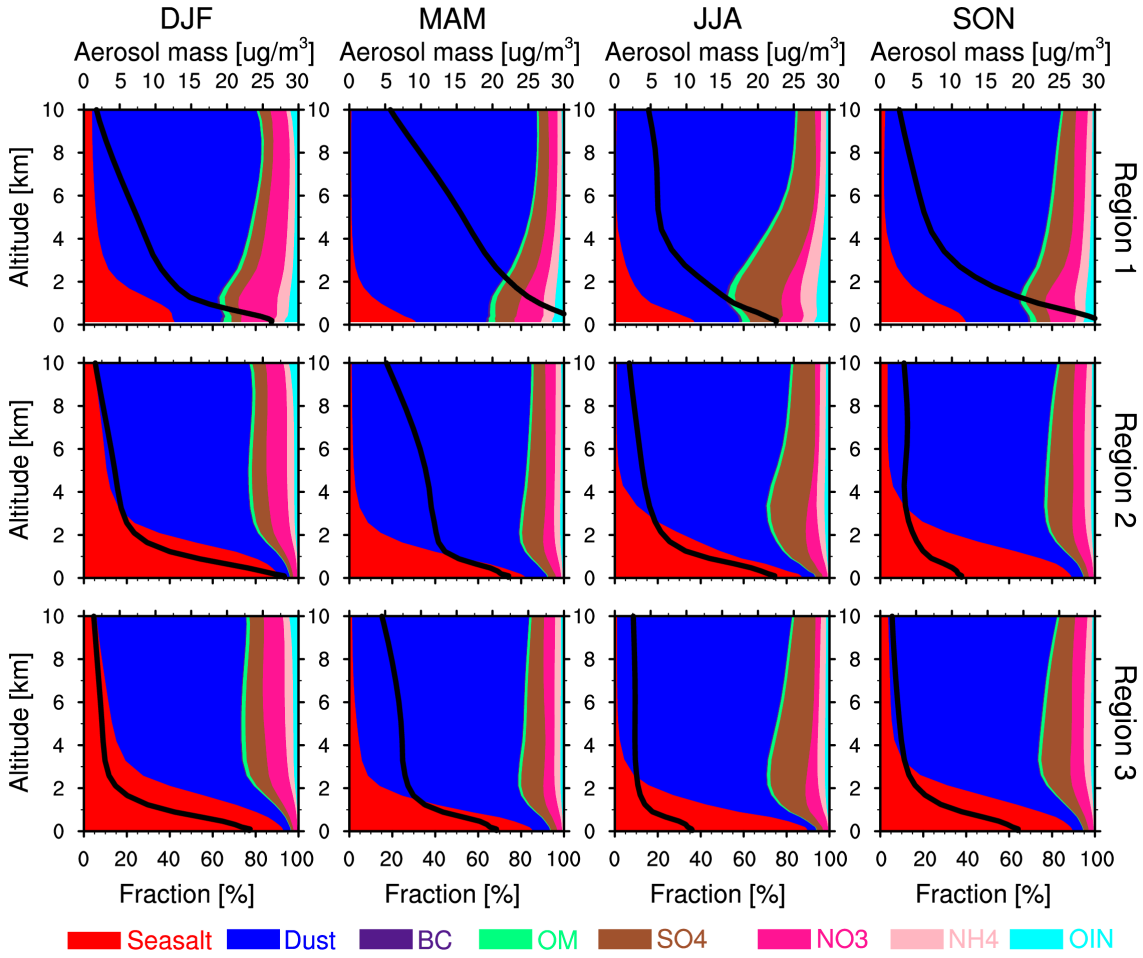


**Figure 14** Vertical distributions of seasonal mean aerosol mass (black solid line; upper X-axis) and its composition fraction (colored shade-contour; lower X-axis) from the WRF-Chem simulation averaged for the period 2010-2014 over three sub-regions as shown in Fig. 4.

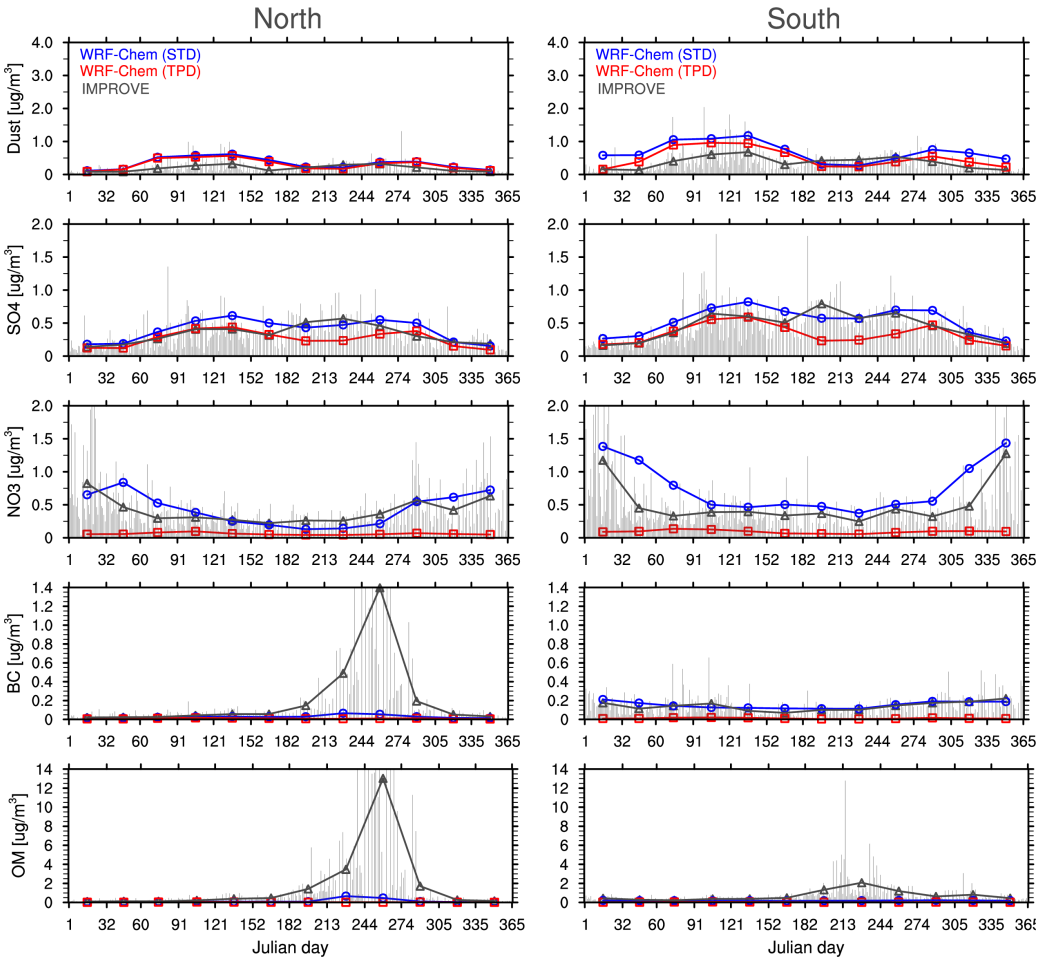


**Figure 15** Daily mass concentrations of fine-mode ($PM_{2.5}$) dust, sulfate, nitrate, BC, and OM averaged for the period 2010-2014 at the IMPROVE sites over the Northwest and Southwest U.S. (shown in Fig. 1) from the IMPROVE observation (vertical gray bars) and the monthly average of the IMPROVE observation (gray triangles) and the corresponding WRF-Chem standard simulation (STD; blue dots) and the sensitivity simulation without North American emissions (TPD; red dots).